

An Exact Hypergraph Matching Algorithm for Posture Identification in Embryonic *Caenorhabditis elegans*

Andrew Lauziere^{1,2,*}, Ryan Christensen², Hari Shroff², Radu Balan^{1,3}

1 Department of Mathematics, University of Maryland, College Park, 4176 Campus Drive College Park MD, 20742-4015, USA

2 Laboratory of High Resolution Optical Imaging, National Institute of Biomedical Imaging and Bioengineering, National Institutes of Health, 13 South Drive, Room G800 Bethesda MD, 20892, USA

3 ACenter for Scientific Computation and Mathematical Modeling (CSCAMM), University of Maryland, College Park, 8169 Paint Branch Drive College Park MD, 20742-4015, USA

* lauziere@umd.edu

Abstract

Point-set matching is a common task in computer vision. Many matching applications feature affine point transformations which can be adequately modeled via lower order objective functions [1, 2]. However, point-set matching tasks may require richer detail in order to characterize underlying relationships. Hypergraphs, an extension of traditional graphs, have emerged to more intricately model relationships between points. Existing hypergraphical point-set matching methods are limited to heuristic algorithms which do not easily scale to handle higher degree hypergraphs [3–5]. Our proposed algorithm, *Exact Hypergraph Matching (EHGM)*, adapts the classical branch-and-bound paradigm to dynamically identify a globally optimal correspondence between point-sets under an arbitrarily intricate hypergraphical model. *EHGM* is applicable to conservatively sized ($n \leq 20$) point-set matching problems in which relationships between points require increased context to adequately characterize. The methodology is motivated by *Caenorhabditis elegans*, a model organism used frequently in developmental biology and neurobiology [6–9]. The *C. elegans* embryo can be used for cell tracking studies to understand how cell movement drives the development of specific embryonic tissues. However, twitching due to muscular activity in late-stage embryos invalidates traditional cell tracking approaches. The embryo possesses a small set of cells which together act as fiducial markers to approximate the coiled embryo’s posture, serving as a frame of reference to track cells of various tissues during late-stage embryogenesis [10]. Current approaches to posture identification rely on time-consuming manual efforts by trained users which limits the efficiency of subsequent cell tracking. *EHGM* with biologically inspired hypergraphical models identifies posture more accurately than established point-set matching methods, correctly identifying twice as many sampled postures as a heuristic graphical approach.

Author summary

Object identification is ubiquitous in day-to-day life. Visual information such as shape, location, and other descriptions in conjunction with temporal context often make the

task routine. The progression towards automation requires the encoding of matching problems in a manner amenable to computational methods. Recent research has established efficient methods to approach conventional matching problems. However, the forefront of identification problems requires powerful modeling techniques and efficient algorithms; existing methods have not been adequately adapted to handle identification tasks beyond standard point transformations. *EHGM* enables rich characterizations of relationships between objects via *hypergraphs*. Hyperedges specify interdependencies between objects and in doing so provide additional information to accurately perform automatic identification. Our method returns globally optimal identifications under an arbitrarily complex hypergraphical model. The nematode *Caenorhabditis elegans* (*C. elegans*) motivates *EHGM*; the roundworm is often studied as a model of neurodevelopment. The worm features approximately 550 cells upon hatching; we focus on a set of 20 which are used to approximate the worm’s posture as it elongates inside the eggshell. Posture identification is challenging due to the worm’s sudden bouts of movement in late-stage development. *EHGM* in conjunction with hypergraphical models using biologically motivated geometric features identify posture more accurately than graphical methods, demonstrating the method’s efficacy while presenting a paradigm for similarly challenging identification tasks.

Introduction

Graphs are abstract mathematical structures used to model observed phenomena across domains. They often arise in computer vision, where vertices represent detected facets of images and edges describe relationships between pairs of vertices. User defined attributes characterize the vertices and edges, such as coordinate positions or shape descriptions and lengths of chords connecting vertices, respectively. Specified attributes give insight to observable relationships between vertices and allow for structural analyses of graphs. Graph matching is the optimization problem defined by the search for a correspondence of vertices between a pair of attributed graphs. Graphs are limited in their expressive power as edges can only relate pairs of vertices; hypergraphs extend the definition of an edge to a hyperedge which specifies a relationship among an arbitrary number of vertices. The number of vertices aligned by the most comprehensive hyperedge defines the degree of a hypergraph. Hypergraph matching then concerns finding an optimal vertex correspondence between pairs of attributed hypergraphs. Hypergraph matching allows for the modeling of highly interdependent point-set matching applications by enabling the use of rich features comprising multiple vertex assignments simultaneously.

Here we present *Exact Hypergraph Matching* (*EHGM*), which exactly solves hypergraph matching for hypergraphs of arbitrary degree. While hypergraph matching is \mathcal{NP} -hard [11], *EHGM* enables great flexibility in modifying the optimization objective in pursuit of an effective contextualization of relationships of points between sets. This work fills multiple gaps in the point-set matching literature. Foremost, the paradigm is able to exactly solve point-set matching problems of arbitrary intricacy. Recent methods for graph matching and lower-degree hypergraph matching focus on heuristic solutions which offer no guarantee on performance [1–5]. Exactness allows for a more rigorous analysis of a hypergraphical point-set matching model than is possible using heuristic techniques. The guarantee of a globally optimal correspondence allows an iterative tuning of the underlying model in pursuit of accurate characterization, whereas the output of a heuristic algorithm could be incorrect due either to the stochasticity of the search or to inadequacy of the optimization objective. Furthermore, recent hypergraph matching methodology [3–5] is limited to simpler objective formulations, whereas *EHGM* supports hypergraphs of arbitrary degree. Indeed, our contributions

enable *EHGM* to approach conservatively sized ($n \leq 20$) challenging point-set matching tasks. The method yields globally optimal correspondences while allowing the comparison of expressive and modifiable hypergraphical objective function formulations.

EHGM is used to model *posture* in embryonic *Caenorhabditis elegans* (*C. elegans*), a small, free-living roundworm. The nematode features approximately 550 cells upon hatching, including a set of twenty *seam cells* and two associated neuroblasts. The seam cells and neuroblasts form in lateral pairs along the left and right sides of the worm, resulting in eleven pairs upon hatching [7]. The neuroblasts appear in the final hours of development, just prior to hatching. The pairs of cells are named, posterior to anterior: *T*, *V6*, *V5*, *Q* (neuroblasts), *V4*, *V3*, *V2*, *V1*, *H2*, *H1*, and *H0*. Each pair's left and right cell is named accordingly; for example, *H1L* and *H1R* comprise the *H1* pair (Fig 1-A). The joint identification of seam cells and neuroblasts approximates the coiled posture, allowing for traditional frame-to-frame tracking of imaged cells belonging to various tissues such as the gut, nerve ring, and bands of muscle (Fig 2-B) [10]. Images are captured in five minute intervals (Fig 1-B) in order to achieve necessary resolution to track cells of other tissues without disturbing embryo development. Current methods for posture identification rely on trained users to manually annotate the imaged nuclei using a 3D rendering tool [12]. The process takes several minutes per image volume and must be performed on approximately 100 image volumes per embryo [10]. Cells are remapped according to splines fitted to the posture (Fig 2-C). The *untwisted* cell positions are then tracked frame-to-frame (Fig 2-D). Manual annotation strategies motivate *EHGM* as established methods for point-set matching fail to adequately capture the relationships between seam cells throughout myriad twists and deformations of the developing embryo.

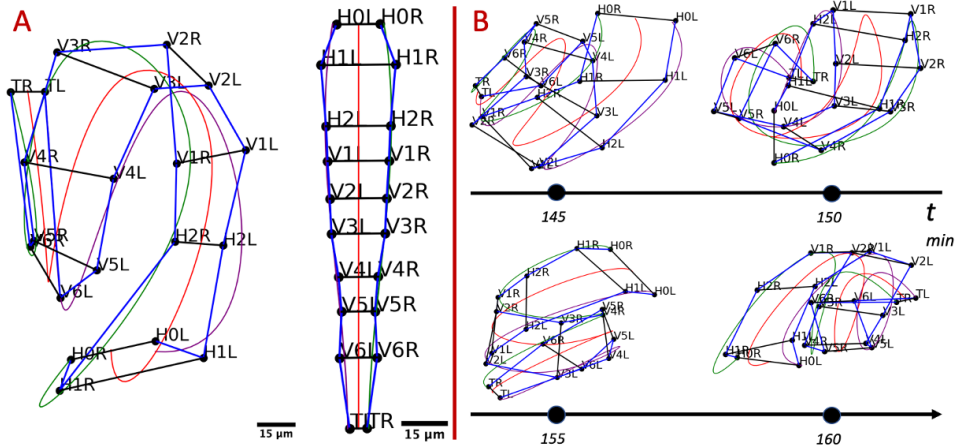


Fig 1. High spatial resolution, low temporal resolution imaging necessitates posture identification. A: Manually identified and seam cell nuclei from an imaged *C. elegans* embryo. The cells form in pairs; they are labelled posterior to anterior: *T*, *V6*, ..., *H0*. Natural cubic splines through the left and right-side seam cells estimate the coiled body. The left image depicts identified nuclei connected to outline the embryonic worm. The fit splines are used to *untwist* the worm, generating the remapped straightened points in the diagram on the right. B: Labelled nuclear coordinates from a sequence of four images. The embryo repositions in the five minute intervals between images, causing failure of traditional tracking approaches.

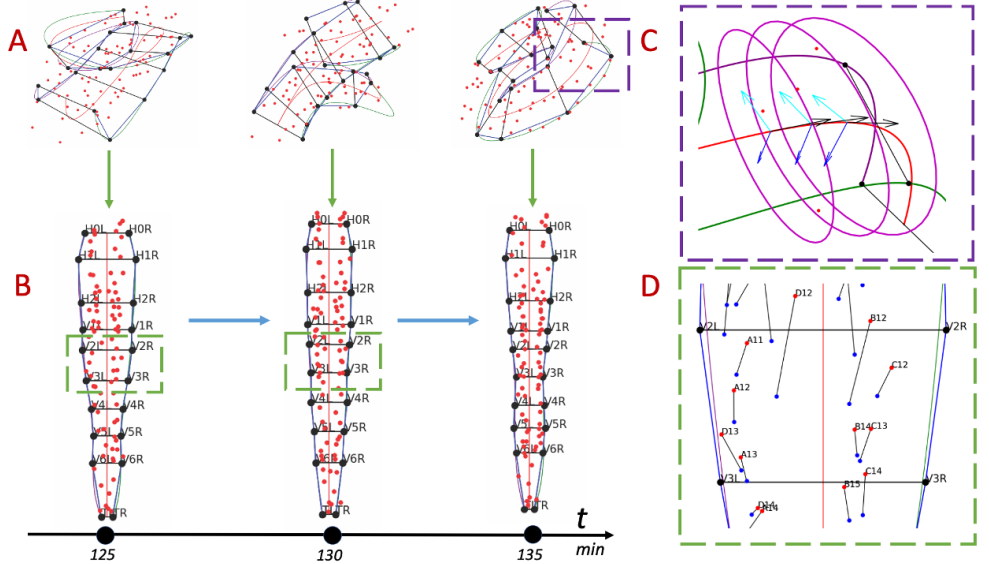


Fig 2. Posture identification allows the tracking of other cells during late-stage embryogenesis. A: Seam cell nuclei coordinates (black) and muscle nuclei coordinates (red) in a sequence of three sequential volumetric images. The untwisting process (green arrows) uses the seam cells to remap muscle coordinates to a common frame of reference. B: The remapped muscle nuclei are tracked frame-to-frame (blue arrows). C: A higher magnification view from the right coordinate plot of A. The left, right, and midpoint splines are used to create a change of basis defined by the tangent (black), normal (blue), and binormal (cyan) vectors. Ellipses are inscribed along the tangent of the midpoint spline, approximating the skin of the coiled embryo. D: A portion of the left (red) and center (blue) remapped muscle coordinates. Black lines connect the coordinates, frame-to-frame.

EHGM uses hypergraphical models comprising biologically driven geometric features to more accurately identify posture than established graphical methods. The limited expressive power of graphical models hinders accurate seam cell identification; graphical models accurately identify posture in 27% of samples compared to 56% using a hypergraphical model. User labelling of the posterior-most seam cell nuclei improves the success of hypergraph matching to correctly identifying all nuclei in 77% of samples. The improved accuracy in posture identification attributed to high-degree hypergraphical modeling solved via *EHGM* paves a path toward automatic posture identification while presenting a general framework for approaching similarly challenging point-set matching tasks.

Results

EHGM deviates from recent graph matching and hypergraph matching methodology as an exact method, guaranteeing convergence to a globally optimal solution [1–5]. The \mathcal{NP} -hardness of both graph matching and hypergraph matching has caused research to concentrate on efficiently scaling heuristic methods. Heuristic hypergraph matching methods approximate the assignment matrix using the dissimilarity tensor [3, 4] whereas *EHGM* builds upon the seminal branch-and-bound algorithm [13]. The branch-and-bound paradigm recursively commits partial assignments while solving successive subproblems within the search space. Each branch then upper bounds the

minimum objective, allowing a pruning of the subsequent set of branches. The method converges upon a globally optimal solution as the bound tightens to the optimum; the search space is implicitly explored by narrowing down the search space to the set of global optimums. *EHGM* extends the methodology to branch and prune based upon a given hypergraphical model. A k -tuple of identities at branch m are greedily selected while another step encapsulates the full hypergraphical objective upon selection. In context, $k=2$ seam cell identities are assigned at each branch starting with the tail pair cells TL and TR . The successive pair cells, $V6L$ and $V6R$, are assigned given the established cells and hypergraphical relationships accessible with the hypothesized identities. Fig 3 depicts *EHGM* applied to the sample image depicted in Fig 1-A. The initial pair ($k=2$) is selected, instantiating a search tree (Fig 3-A). Successive seam cell identities are partially assigned according to the given hypergraphical model in a pair-wise fashion. Each branch greedily queues hypothesized point-pair assignments conditioned on the previous branch assignments (black arrows within a branch). The next leading $V6$ pair (Fig 3-E) is chosen upon exhaustion of the leading hypothesized $V6$ pair (Fig 3-B). *EHGM* continues the recursion to implicitly identify a globally optimal posture under the given hypergraphical model; each possible initial pair will follow this illustrated process subject to pruning of the minimizing posture accessed via the hypothesized tail pair in Fig 3-A.

Posture was predicted according to a graphical model, denoted *QAP* (SI-*QAP*), and two prospective hypergraphical models: *Pairs* (SI-*Pairs*) and *Posture* (SI-*Posture*). *Pairs* uses degrees four and six hyperedges to more strongly model local regions of the embryo than is possible with graphical methods which rely on second degree relationships. *Posture* further demonstrates the capabilities of *EHGM* by including a degree n_1 hyperedge to maximize context in evaluating a hypothesized posture. Geometric features such as pair-to-pair rotation angles and left-right flexion angles were developed to quantify seam cell identification costs. Each angle or distance requires multiple seam cell identities in tandem to calculate, leveraging the hypergraphical model to contextualize posture. *KerGM* [2], a leading algorithm for heuristic graph matching, was applied to posture identification. The algorithm used the same connectivity matrix as *QAP*, but processed results frame-to-frame serially, relying on the correct posture identification at the prior image as input to search. *EHGM* models matched to an estimated template as opposed to identified coordinates in the prior image (SI-Model Fitting).

Fig 4 demonstrates the posture identification task applied to the first two sampled images in Fig 1-B. A series of four increasingly intricate models applied to the sample images are illustrated. Linear models (Fig 4-A & Fig 4-B) are ill-equipped to identify posture due to the repositioning of the embryo between successive images. Graphical models such as *QAP* (Fig 4-C & Fig 4-D) associate local seam cells via edges (purple). Edge-wise features such as lengths and widths vary if the embryo coils tightly, but are otherwise approximately static frame-to-frame. However, the similarity in these measurements throughout the embryo yields a model incapable of differentiating portions of the embryo. Hypergraphical models *Pairs* (Fig 4-E & Fig 4-F) and *Posture* (Fig 4-G & Fig 4-H) use aforementioned hyperedges to more strongly characterize embryonic posture.

Annotators curated a dataset of seam cell nuclei center coordinates from 16 imaged embryos. Each imaged embryo yielded approximately 80 image volumes for a total of 1264 labelled seam cell coordinate sets. Homogeneity in *C. elegans* embryo development allowed use of samples spanning multiple embryos to fit models via a leave-one-out approach (SI-Model Fitting, SI-*C. elegans* Posture Modeling). *EHGM* allows for known correspondences, henceforth referred to as *seeds*, to be given as input prior to search initialization. The algorithm was evaluated both in a traditional point-set matching

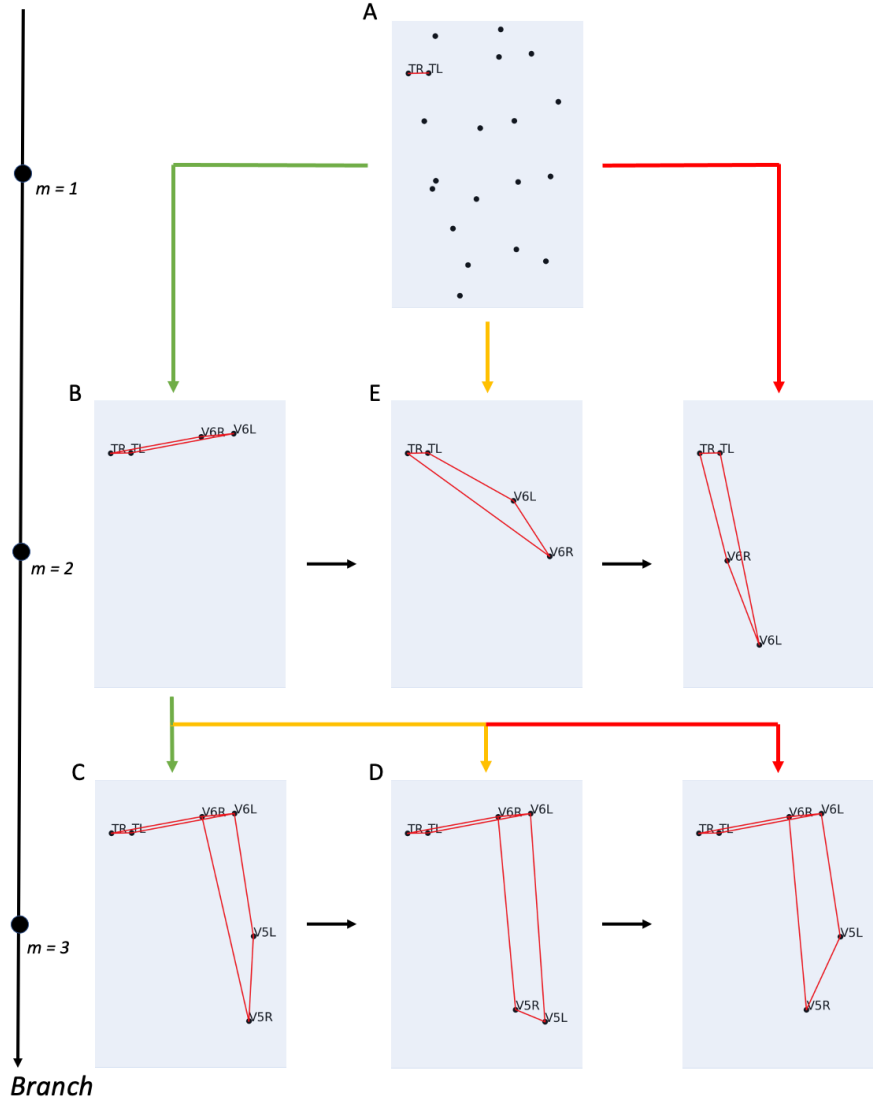


Fig 3. EHGM applied to the sample image depicted in Fig 1-A. A: Two points are selected at the initial branch for TL and TR , respectively. Candidates for the successive pair, $V6L$ and $V6R$, are queued based on hypergraphical relationships between the established cell identities TL and TR and each hypothesized $V6$ pair (lower costs are green to higher costs in red). B: The leading hypothesis at branch $m=2$ given the initial branch pair is chosen. The recursion continues to queue $V5$ pair choices at branch $m=3$. Black arrows within branch m specify the ordering of the branch given established cell assignments. Each branch creates a new subproblem of completing the posture given partially assigned identities. C: The tree continuing from the $V5$ pair hypothesis is fully explored according to the established recursion. D: The next leading $V5$ hypothesis is initiated upon exhaustion of the subtree formed at panel C. E: Implicit enumeration of the subtree formed at panel B causes the search to progress to the second leading $V6$ hypothesis.

scenario given no *a priori* information, and in a series of seeded simulations. Seeded trials assumed incrementally more pairs given sequentially from the tail pair, T , to the

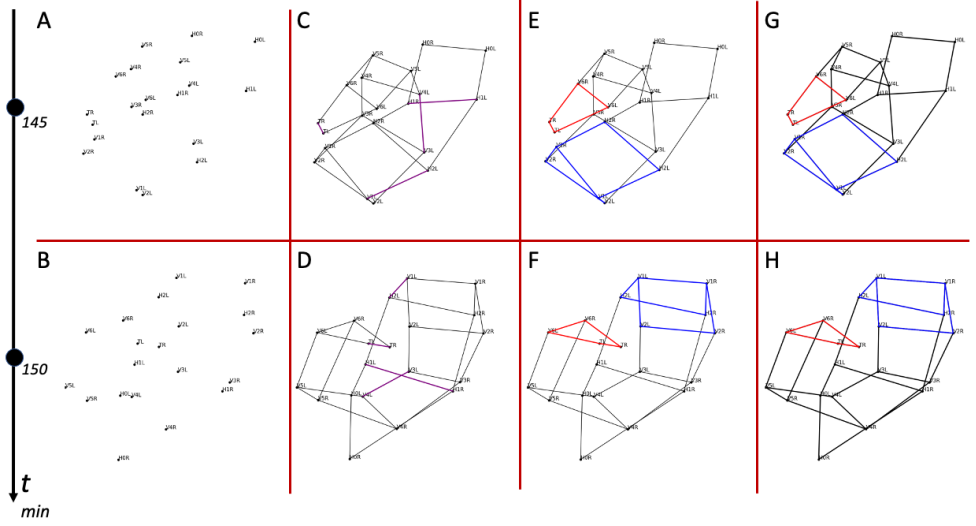


Fig 4. Posture identification applied to two successive images in Fig 1-B according to a series of increasingly intricate models. The embryo repositions between images. A & B: Linear models cannot quantify relationships between seam cells; posture identification is impossible without context of neighboring cell identities. C & D: A graphical model (*QAP* specifies edges (purple) between pairs of seam cell nuclei. Edge lengths are relatively static frame-to-frame, but the similarity of edge lengths throughout the embryo causes the edges to have a weak signal in identifying seam cells. E & F: The *Pairs* model uses degrees four (red) and six (blue) hyperedges to model a greater local context than is possible in a graphical model. G & H: The *Posture* model extends the *Pairs* model to use a degree n_1 (black) hyperedge to evaluate all seam cell assignments jointly.

fourth pair, V_4 (or Q for $n_1=22$ samples).

EHGM is able to store complete assignments encountered during the search as it compares against the current solution at the final branch. This allowed for an analysis of the similarity between leading solutions and progressively higher cost solutions encountered during search. Results highlight the percentage of samples in which the correct posture (correct identification of *all* seam cells) is returned as the minimizer (Table 1). The top x accuracy describes the percentage of samples that are in the top x hypothesized postures returned; i.e. the top 1 accuracy describes the percentage of samples in which the correct seam cell identification was returned, and the top 3 accuracy is the percentage of samples in which the correct assignment was in the top 3 hypotheses returned by the search. Top 1 and top 3 accuracy percentages as well as the median runtime are reported alongside the median cost ratio, defined as the ratio of the correct posture's objective to the returned hypothesized posture. A cost ratio greater than one implies the search yielded a lower cost posture than the known biologically correct posture, suggesting the model is not aptly describing the relationship between seam cells.

KerGM identified 27% of sampled postures correctly, outperforming *QAP* (Table 1). *Pairs* and *Posture* more effectively identified posture with 52% and 56% top 1 accuracies, respectively. Both hypergraphical models also reported a median cost ratio of 1.00, compared to 1.28 of *QAP*, suggesting the hypergraphical representations of coiled posture provided enhanced discriminatory power across samples. The hypergraphical models demonstrated small trade-offs between accuracy and runtime.

The *Posture* model's posture-wide features improved accuracy over *Pairs*, 56% to 52%, in exchange for longer median runtime, 60 minutes to 43 minutes. Differences between the top 1 and top 3 accuracies illustrate the challenge in posture identification. The cost minimizing hypotheses were often similar to minimizers. Notably, the *Posture* model returned the correct posture in the top 3 hypotheses in approximately 67% of samples, an approximate 20% increase in relative accuracy over the top 1 percentage.

	Top 1 (%)	Top 2 (%)	Top 3 (%)	Top 5 (%)	Top 10 (%)	R (minutes)	CR
<i>KerGM</i>	27	27	27	27	27	.01	
<i>QAP</i>	10	14	15	16	16	5.97	1.28
<i>Pairs</i>	52	60	63	65	65	43.22	1.00
<i>Posture</i>	56	65	67	68	68	60.35	1.00

Table 1. Posture-wide hypergraphical model achieves highest accuracy. Posture identification accuracies across all 1264 samples. Rows correspond to models. The first columns list the top x accuracy as a percentage of samples. The column titled R shows the median runtime of each model in minutes. CR reports the median cost ratio, defined as the ratio of the correct posture cost to the returned posture cost.

Posture identification results were stratified by the presence of the Q neuroblasts; 875 samples contain only the seam cells while 389 of the 1264 samples contain the Q neuroblasts. Table 2 depicts the findings presented in Table 1 split by Q neuroblast presence. All methods achieved a higher accuracy on Q samples. Notably, the *Posture* model's top 3 accuracy is higher than that of *Pairs* on the Q pair data: 60% to 82%. The extra pair of coordinates provided substantial context, further defining the coiled shape and empowering the penalization of incorrect postures.

	Top 1 (%)	Top 2 (%)	Top 3 (%)	Top 5 (%)	Top 10 (%)	R (minutes)	CR
<i>KerGM</i>	25	25	25	25	25	.01	
<i>QAP</i>	7	10	11	12	12	4.81	1.36
<i>Pairs</i>	44	51	55	57	58	34.25	1.04
<i>Posture</i>	48	57	60	61	62	51.12	1.00

	Top 1 (%)	Top 2 (%)	Top 3 (%)	Top 5 (%)	Top 10 (%)	R (minutes)	CR
<i>KerGM</i>	35	35	35	35	35	.01	
<i>QAP</i>	19	25	26	26	26	9.66	1.16
<i>Pairs</i>	71	80	82	82	82	56.58	1.00
<i>Posture</i>	72	81	82	83	83	72.60	1.00

Table 2. Hypergraphical models leverage Q neuroblasts to identify posture. The samples are split according to the absence (top) or presence (bottom) of the Q neuroblasts, which form in the last two hours of development. There are 875 $n_1=20$ cell samples and 389 $n_1=22$ Q samples. Reported methods more accurately identify embryonic posture in the Q samples, suggesting the increased continuity along the body of the embryo allows for more consistent posture identification.

The top x percentage accuracy metric reflects the need to correctly identify *all* seam cells in order to recover the underlying posture, but does not distinguish between hypotheses that are incorrect due to one cell identity swap or a more systemic modeling inadequacy. A qualitative analysis highlighted a few themes among incorrectly predicted postures. The foremost errors concern the tail pair cells, *TL* and *TR*; spurious identifications occurred when the tail pair coiled against another the body of the embryo, causing one tail cell identity to be interchanged with a cell of a nearby body pair. The variance of feature measurements in the posterior region (SI-*QAP*, SI-*Pairs*)

resulted in similar costs for postures with minor differences about the posterior region. The prevalence of such errors motivated further analysis of seeding posterior seam cell identities prior to search.

Seeded experiments specifying nuclear identities provided *a priori* with information starting with the tail pair, and incrementally identified more pairs in the posterior region. Each experiment was given five minutes of maximum runtime; a semi-automated solution requiring more runtime was deemed infeasible. Top 1 and top 3 accuracy percentages are reported across models and simulations in Table 3. Seeding of pairs yielded decreasing marginal improvements to accuracy and runtime. Fig 5 depicts top 1 accuracies and median runtimes across seeded experiments for the *Pairs* and *Posture* models split by Q pair labelling. Particularly, seeding the first two pairs, T and $V6$, greatly reduces the median runtime while also netting the largest gains in top 1 accuracy, partially attributable to *EHGM* converging in the given timeframe.

	Top 1 (%)						Top 3 (%)					
	None	T	T-V6	T-V5	T-V4	None	T	T-V6	T-V5	T-V4		
<i>QAP</i>	9	10	22	29	37	13	15	27	35	43		
<i>Pairs</i>	34	49	72	79	84	38	54	77	83	87		
<i>Posture</i>	25	36	68	79	84	27	39	73	84	87		

Table 3. Seeding posterior pair identities promotes accurate posture identification and reduces runtime. Top 1 and top 3 seeded posture identification accuracies across all samples. All trials had a five-minute maximum runtime. The rows again correspond to each model. Columns specify which pairs were given as seeds prior to search. The *None* columns recreate the original no information task. The subsequent columns specify which pairs are correctly identified prior to search.

Discussion

We have presented *EHGM* as a dynamic and effective tool for intricate point-set matching tasks. The hypergraph matching algorithm provides a method in which to gauge the efficacy of modeling point correspondences in conservatively-sized problems; problems featuring larger numbers of points likely contain the context required to match adequately via lower degree models. For example, postures in samples containing Q nuclei were more accurately identified across models, but the largest marginal gain in accuracy came from *QAP* ($d = 2$) to *Pairs* ($d = 4, 6$). The results suggest that added context throughout the embryo would further improve posture identification accuracy, reducing the reliance on higher degree (and thus more computationally expensive) hypergraphical objectives. *EHGM* specifically addresses a gap in literature concerning challenging point-set matching applications in which domain-specific features lead to rigorously testable models. Seeding allows a wider range of problems to be approached, and mitigates the computational expense of the algorithm for scenarios featuring larger point-sets.

Posture identification in embryonic *C. elegans* is a challenging problem benefiting from high degree hypergraphical modeling. *EHGM* equipped with biologically inspired hypergraphical models led to substantial improvement in posture identification. The top 1 accuracy doubled from 27% with a graphical model to 56% via the *Posture* model (Fig 1). The top 3 accuracy rate improved to 67%, highlighting the challenge in precisely specifying the coiled embryo due to the similarity of competing posture hypotheses. The presence of Q neuroblasts further contributed to accurate posture identification. The added context empowered the *Posture* model to identify the correct

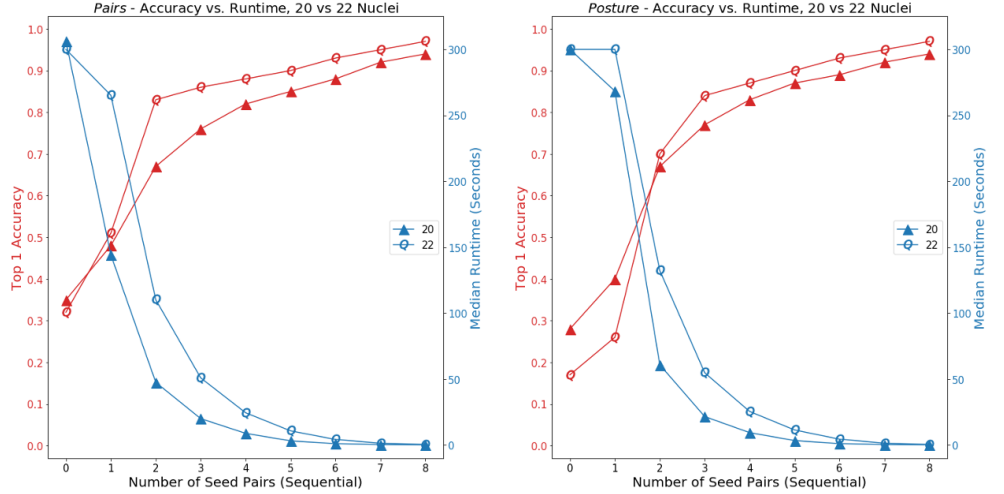


Fig 5. Evaluating the *Pairs* and *Posture* models as seam cell identities were seeded. The *Pairs* and *Posture* models top 1 accuracies and median runtimes by Q pair labelling. Posterior pair seeding drastically improved top 1 accuracy and reduced runtime when applying both models. Q pair samples required more runtime ($n_1=22$ as opposed to $n_1=20$), but the added context improved posture identification accuracy. The majority of samples converged within 5 minutes when seeded with the T and $V6$ pairs of nuclei.

posture in 82% of Q samples. Seeding allows for the strengths of *EHGM* to compensate for the most challenging aspect of posture identification. The posterior region of the embryonic worm is especially flexible and contributes to the majority of reported errors. Feature engineering stands to create hypergraphical models more capable of reliable posture identification, particularly in contextualizing the posterior region. The method and application outline a protocol for challenging point-set matching tasks.

Methods

Highly interdependent point-set matching is achieved by expressing the task as hypergraph matching. The traditional point-set matching problem concerns two sets of points: an established point-set of size n_1 and a second set of unidentified points of size n_2 . The goal is to obtain a one-to-one correspondence between sets of points that is optimal according to an objective function f . The objective measures the dissimilarity arising from a permutation aligning the vertices between point-sets given an attributed hypergraphical representation.

Hypergraph Matching

The first input hypergraph of size n_1 is assumed to have a maximum hyperedge degree n_1 , with identified points: l_i , $i = 1, 2, \dots, n_1$. The set of points to be identified: l'_j , $j = 1, 2, \dots, n_2$ are matched in a manner such that the objective f is minimized subject to one-to-one constraints. *EHGM* assumes $n_1 \leq n_2$, i.e., the algorithm can account for extraneous points but the specified hypergraphical form must be completely satisfied by the second point-set of size n_2 . A assignment matrix $X \in \mathcal{X}$ is used to designate a matching between sets:

$$\mathcal{X} = \{X \in \{0,1\}^{n_1 \times n_2} : \forall j, \sum_{i=1}^{n_1} x_{ij} \leq 1, \forall i \sum_{j=1}^{n_2} x_{ij} = 1\}$$

where the binary variable $x_{l_i l'_j} = 1$ if vertex l_i in the original hypergraph is assigned to point l'_j . The hypergraph dissimilarity tensor:

$$\mathbf{Z} \in \mathfrak{R}_{\geq 0}^{\underbrace{n_1 \times n_2}_{1} \times \underbrace{n_1 \times n_2}_{2} \dots \underbrace{n_1 \times n_2}_{n_1}}$$

fully captures the dissimilarity up to degree n_1 arising between the matching: $(l_1, l_2, \dots, l_{n_1}) \mapsto (l'_1, l'_2, l'_3, \dots, l'_{n_1})$. Then, for a given permutation matrix X , the hypergraph matching objective can be written in a condensed form, assuming $l_1 < l_2 < \dots < l_{n_1}$:

$$f(X|\mathbf{Z}) = \sum_{l_1=1}^{n_1} \sum_{l'_1=1}^{n_2} \sum_{l_2=l_1+1}^{n_1} \sum_{l'_2=1}^{n_2} \dots \sum_{l_{n_1}=l_{n_1-1}+1}^{n_1} \sum_{l'_{n_1}=1}^{n_2} \mathbf{Z}_{l_1 l'_1 l_2 l'_2 \dots l_{n_1} l'_{n_1}} x_{l_1 l'_1} x_{l_2 l'_2} \dots x_{l_{n_1} l'_{n_1}} \quad (1)$$

Assume the formulation of f in Eq 1 can be decomposed according to each hyperedge degree $d = 1, 2, \dots, n_1$. The dissimilarity tensor \mathbf{Z} evaluated at an assignment can then be rewritten as a summation of n_1 dissimilarity tensors of dimension $2, 4, \dots, 2d, \dots, 2n_1$, each measuring dissimilarity between degree d hyperedges, respectively. Define $\mathbf{Z}^{(d)}$ as the tensor mapping the dissimilarity for the degree d hyperedges. Then \mathbf{Z} can be written as a summation across n_1 tensors $\mathbf{Z}^{(d)}$. The optimization problem can ultimately be expressed as in Eq 2.

$$\begin{aligned} f(X|\mathbf{Z}^{(1)}, \mathbf{Z}^{(2)}, \dots, \mathbf{Z}^{(n_1)}) &= \sum_{l_1=1}^{n_1} \sum_{l'_1=1}^{n_2} \mathbf{Z}_{l_1 l'_1}^{(1)} x_{l_1 l'_1} + \sum_{l_1=1}^{n_1} \sum_{l'_1=1}^{n_2} \sum_{l_2=l_1+1}^{n_1} \sum_{l'_2=1}^{n_2} \mathbf{Z}_{l_1 l'_1 l_2 l'_2}^{(2)} x_{l_1 l'_1} x_{l_2 l'_2} + \dots \\ &+ \sum_{l_1=1}^{n_1} \sum_{l'_1=1}^{n_2} \sum_{l_2=l_1+1}^{n_1} \sum_{l'_2=1}^{n_2} \sum_{l_3=l_2+1}^{n_1} \sum_{l'_3=1}^{n_2} \mathbf{Z}_{l_1 l'_1 l_2 l'_2 l_3 l'_3}^{(3)} x_{l_1 l'_1} x_{l_2 l'_2} x_{l_3 l'_3} + \dots \\ &+ \sum_{l_1=1}^{n_1} \sum_{l'_1=1}^{n_2} \dots \sum_{l_{n_1}=l_{n_1-1}+1}^{n_1} \sum_{l'_{n_1}=1}^{n_2} \mathbf{Z}_{l_1 l'_1 \dots l_{n_1} l'_{n_1}}^{(n_1)} x_{l_1 l'_1} \dots x_{l_{n_1} l'_{n_1}} \end{aligned} \quad (2)$$

Exact Hypergraph Matching

EHGM extends the branch-and-bound paradigm to exactly solve hypergraph matching. The algorithm performs the search in the permutation space \mathcal{X} subject to a given branch size k which specifies the number of vertices assigned at each branch. A size n_1 hypergraph will require $M := \frac{n_1}{k}$ branch steps, where branch m concerns the assignment of vertices $((m-1)k+1, (m-1)k+2, \dots, mk)$; vertices $1, 2, \dots, mk$ have been assigned upon completion of the m^{th} branch. The set \mathbf{P} contains all possible permutations of the indices of the unordered point set, $|\mathbf{P}| = \frac{n_2!}{(n_2-k)!}$. \mathbf{P} is incrementally subset into queues $\mathbf{Q}_m \subseteq \mathbf{P}$ at branches $m = 1, 2, \dots, M$ at each branching. The queue \mathbf{Q}_m is subset according to both a pruning rule which eliminates permutations leading to a suboptimal solution as well as the one-to-one constraints of \mathcal{X} . The search converges to a global optimum upon the implicit enumeration of $\mathbf{Q}_1 = \mathbf{P}$.

The objective function f is further stratified according to the branch size k . Lower degree ($d \leq 2k$) hyperedge dissimilarity tensors are computed prior to search. Branches

comprising k -tuples of vertices are partially assigned in a greedy manner according these lower degree hyperedge dissimilarities via the selection rule H . Later branches accrue higher degree ($d > 2k$) hyperedge dissimilarities which are calculated at time of branching; the intent of the method is to rely on lower degree terms to steer the search towards an optimum in effort to minimize the number of branches explored. The aggregation rule I accrues higher degree hyperedge dissimilarity terms upon branching, further guiding the pruning step and ensuring the complete specification of the objective f .

The branching and selection rules are designed to reduce computation performed throughout the search. A partial assignment at branch m :

$\mathbf{K}_m = (l'_{(m-1)k+1}, l'_{(m-1)k+2}, \dots, l'_{mk}) \in \mathbf{Q}_m$ is selected via precomputed lower degree hyperedge dissimilarity tensors $\mathbf{Z}^{(1)}, \dots, \mathbf{Z}^{(2k)}$. A larger branch size k results in a selection rule with larger scope of the optimization landscape, better equipped to place optimal branches earlier in each queue \mathbf{Q}_m at time of branching. However, computing the lower degree dissimilarity tensors prior to search can be prohibitively expensive for larger point-sets.

Selection & Aggregation

The first branch permutation $\mathbf{K}_1 = (l'_1, l'_2, \dots, l'_k) \in \mathbf{Q}_1 = \mathbf{P}$ assigns vertices (l_1, l_2, \dots, l_k) to points $(l'_1, l'_2, \dots, l'_k)$ according to the initial branch selection rule H_1 . Eq 3 defines a cost given dissimilarity tensors $\mathbf{Z}^{(1)}, \mathbf{Z}^{(2)}, \dots, \mathbf{Z}^{(k)}$ according to a permutation \mathbf{K}_1 . The k pairs of constraints given by the branch m and permutation of point indices \mathbf{K}_m : $\{(l_1, l'_1), \dots, (l_k, l'_k)\}$ enables a simplification in the objective formulation.

$$H_1(\mathbf{K}_1 | \mathbf{Z}^{(1)}, \mathbf{Z}^{(2)}, \dots, \mathbf{Z}^{(k)}) := \sum_{i_1=1}^k \mathbf{Z}_{l_{i_1} l'_{i_1}}^{(1)} + \sum_{i_1=1}^k \sum_{i_2=i_1+1}^k \mathbf{Z}_{l_{i_1} l'_{i_1} l_{i_2} l'_{i_2}}^{(2)} + \dots + \sum_{i_1=1}^k \sum_{i_2=i_1+1}^k \dots \sum_{i_k=i_{k-1}+1}^k \mathbf{Z}_{l_{i_1} l'_{i_1} l_{i_2} l'_{i_2} \dots l_{i_k} l'_{i_k}}^{(k)} \quad (3)$$

Subsequent branches $m = 2, 3, \dots, M$ then use the general selection rule H_m to order the permutations of the m^{th} branch: $\mathbf{K}_m = (l'_{(m-1)k+1}, l'_{(m-1)k+2}, \dots, l'_{mk}) \in \mathbf{Q}_m$. Branch \mathbf{K}_m incurs a selection rule cost H_m according to Eq 4 comprising lower degree hyperedge dissimilarities for assignments both within branch m and the assignments between branches $1, 2, \dots, m-1$ and branch m . The partial assignment constraints \mathbf{K}_m allow further simplification of notation; the reversed order of summation indices satisfies the criteria that only hyperedge dissimilarities pertaining to branch m assignments are considered via H_m .

$$H_m(\mathbf{K}_m | \mathbf{K}_1, \dots, \mathbf{K}_{m-1}, \mathbf{Z}^{(1)}, \dots, \mathbf{Z}^{(2k)}) := \sum_{i_1=(m-1)k+1}^{mk} \mathbf{Z}_{l_{i_1} l'_{i_1}}^{(1)} + \sum_{i_2=(m-1)k+1}^{mk} \sum_{i_1=1}^{i_2-1} \mathbf{Z}_{l_{i_1} l'_{i_1} l_{i_2} l'_{i_2}}^{(2)} + \dots + \sum_{i_3=(m-1)k+1}^{mk} \sum_{i_2=1}^{i_3-1} \sum_{i_1=1}^{i_2-1} \mathbf{Z}_{l_{i_1} l'_{i_1} l_{i_2} l'_{i_2} l_{i_3} l'_{i_3}}^{(3)} + \dots + \sum_{i_{2k}=(m-1)k+1}^{mk} \sum_{i_{2k-1}=1}^{i_{2k}-1} \dots \sum_{i_1=1}^{i_2-1} \mathbf{Z}_{l_{i_1} l'_{i_1} \dots l_{i_{2k}} l'_{i_{2k}}}^{(2k)} \quad (4)$$

The greedy selection rule orders queues \mathbf{Q}_m , but does not account for higher degree ($2k < d \leq n_1$) hyperedge dissimilarities. Precomputing higher degree dissimilarity tensors can be both computationally expensive, and inefficient as ideally only a small percentage of combinations are queried throughout the search. The aggregation rule I_m , $m = 3, 4, \dots, M$ measures the dissimilarity attributable to higher degree ($2k < d \leq mk$) hyperedges accessible due to branch m partial assignments. The aggregation rule updates the cost of branch \mathbf{K}_m assignments, further informing the pruning step to subset the next queue \mathbf{Q}_{m+1} . The greedy selection rule H_m in tandem with the aggregation rule I_m aim to minimize the total computation performed in finding an optimum. The definition I_m follows from the general selection rule H_m , but is applied to the higher degree hyperedge dissimilarities. An intermediate term $\Xi_m^{(d)}$ (Eq 5) measuring the degree d dissimilarities calculable upon assignments of branch m assignments is introduced for simplification of notation. The aggregation rule I_m (Eq 6) can be simply expressed as the $\Xi_m^{(d)}$ terms for degrees $2k < d \leq mk$.

$$\Xi_m^{(d)}(\mathbf{K}_m | \mathbf{K}_1, \mathbf{K}_2, \dots, \mathbf{K}_{m-1}, \mathbf{Z}^{(2k+1)}, \dots, \mathbf{Z}^{(mk)}) := \sum_{i_d=(m-1)k+1}^{mk} \sum_{i_{d-1}=1}^{i_d-1} \dots \sum_{i_1=1}^{i_2-1} \mathbf{Z}_{l_{i_1}l_{i_1}' \dots l_{i_d}l_{i_d}'}^{(d)} \quad (5)$$

$$I_m(\mathbf{K}_m | \mathbf{K}_1, \mathbf{K}_2, \dots, \mathbf{K}_{m-1}, \mathbf{Z}^{(2k+1)}, \dots, \mathbf{Z}^{(mk)}) := \sum_{d=2k+1}^{mk} \Xi_m^{(d)} \quad (6)$$

The m^{th} branch allows for hyperedge dissimilarities up to degree mk concerning the first mk assignments. The M^{th} branch yields a complete assignment, allowing the evaluation of maximum degree n_1 hyperedge dissimilarities. The partitioning and further regrouping of each H_m and I_m as defined fully accounts for the objective f while allowing efficient computation during the search (SI-Hypergraphical Objective Decomposition, SI-Convergence EHGM).

Posture Identification in Embryonic *C. elegans*

Caenorhabditis elegans (*C. elegans*) is a small, free-living nematode found across the world. The worm is often studied as a model of nervous system development due to its relative simplicity [6, 9]. The adult worm features only 302 neurons, the morphology and synaptic patterning of which have been determined via electron microscopy [6]. The complete embryonic cell lineage has also been determined [7]; methods and technology have been developed to allow study of cell position and tissue development in the embryo [14–19]. Systems-level studies of these processes in the embryo may be able to discover larger-scale principles underlying these developmental events.

The roundworm features the set of twenty *seam cells* and two associated neuroblasts (Section-Introduction). Fluorescent proteins are used to label cell nuclei, the seam cell nuclei so that they may be visualized during imaging, e.g. with light sheet microscopy [20]. Volumetric images are captured at five minute intervals in order to capture subcellular resolution without damaging the worm's development [10]. Fig 1-A depicts both coiled (as imaged) and straightened coordinates of the identified seam cell nuclei from an example image volume. Lateral black lines connect nuclei within each pair, while blue lines connect sequential nuclei along the left and right sides of the worm. Natural cubic splines along each side and through pair midpoints estimate the worm's

body. Fig 1-B shows labelled seam cell nuclei coordinates from four sequential images. The worm repositions entirely between images due to the action of muscle cells along the body wall of the embryo. The large movements between images invalidates the application of traditional tracking methodologies to seam cell identification.

The seam cells and neuroblasts together describe anatomical structure in the coiled embryo, acting as a type of “skeleton” outlining its body. Posture identification is crucial for tracking cells belonging to different tissues in late-stage development. *Untwisting* the worm describes the computational process of using the identified seam cell nuclei coordinates to remap coordinates of other imaged cells to a straightened coordinate system [10]. For example, muscle cells form in four bands along the exterior walls of the embryo, comprising approximately 84 cells [7]. Fig 2-A depicts both seam cell nuclei coordinates (black) and the muscle cell nuclei coordinates (red) from three sequential image volumes. Identifying and tracking the muscle cell nuclei as well as those from other tissues is only feasible when using the seam cell nuclei as fiducial markers and untwisting (vertical green arrows). Fig 2-B shows frame-to-frame muscle cell nuclei tracking (blue arrows); remapping the coordinates to a common frame of reference requires the identified posture. Fig 2-C illustrates the untwisting process on a magnified portion of the right coordinate set in Fig 2-A. The remapping uses the left, right, and midpoint splines to establish a change of basis to a straightened coordinate space defined by the tangent (black), normal (blue), and binormal (cyan) vectors. Nuclei encountered are remapped according to the position along the spline and location within the closest inscribed ellipse. Black lines connect cell nuclei in the left frame (red) to their locations in the middle frame (blue); muscle cell names arise from the four bands (A-D), anterior to posterior (Fig 2-D).

Seam cell nuclei appear in the fluorescent images as homogeneous spheroids. Their positions relative to other nuclei and other salient cues present in the image volumes comprise the information that trained users employ to manually identify seam cell nuclei. Fig 6 shows the two rendered fluorescent images from Fig 1-A in Medical Image Processing, Analysis and Visualization (MIPAV), a 3D rendering tool [12]. The interface is used to annotate both seam cell nuclei and track remapped nuclei [10].

We cast seam cell identification as hypergraph matching and use *EHGM* to solve the resulting optimization problem. The traditional point-set matching task requires a labelled point-set and a second unidentified point-set. Higher order features such as bend and twist angles may vary largely frame-to-frame depending on the posture at moment of imaging. However, elongation throughout late-stage development causes macroscopic trends in these geometric features. We estimate a template posture as a composite of feature measurements from a corpus of manually annotated postures (SI-Model Fitting).

The hypergraph matching objective function f describes the assignment of 3D coordinates to cell identities. We apply one graphical objective function and two hypergraphical objective functions, henceforth referred to as models, of increasing complexity to perform seam cell identification. All three models use a pair assignment branching scheme: $k=2$, and *EHGM* partially assigns cell identities posterior to anterior. The initial pair branching rule is also uniform across models. The tail pair seam cells, TL and TR , are the only cells reliably identified using exclusively second order (quadratic) terms; they are notably closer together than other paired cells. There are no unary terms across models; i.e., $\mathbf{Z}^{(1)} = \mathbf{0}$. This is a result of two key facets of the problem: first, the embryo completely repositions between images. The location of a seam cell and its position five minutes later are unrelated (see Fig 1-B). Second, the homogeneity of the nuclear appearances grant no morphologically unique features to discern one from another (see Fig 6).

The simplest model expresses seam cell identification as graph matching, and thus

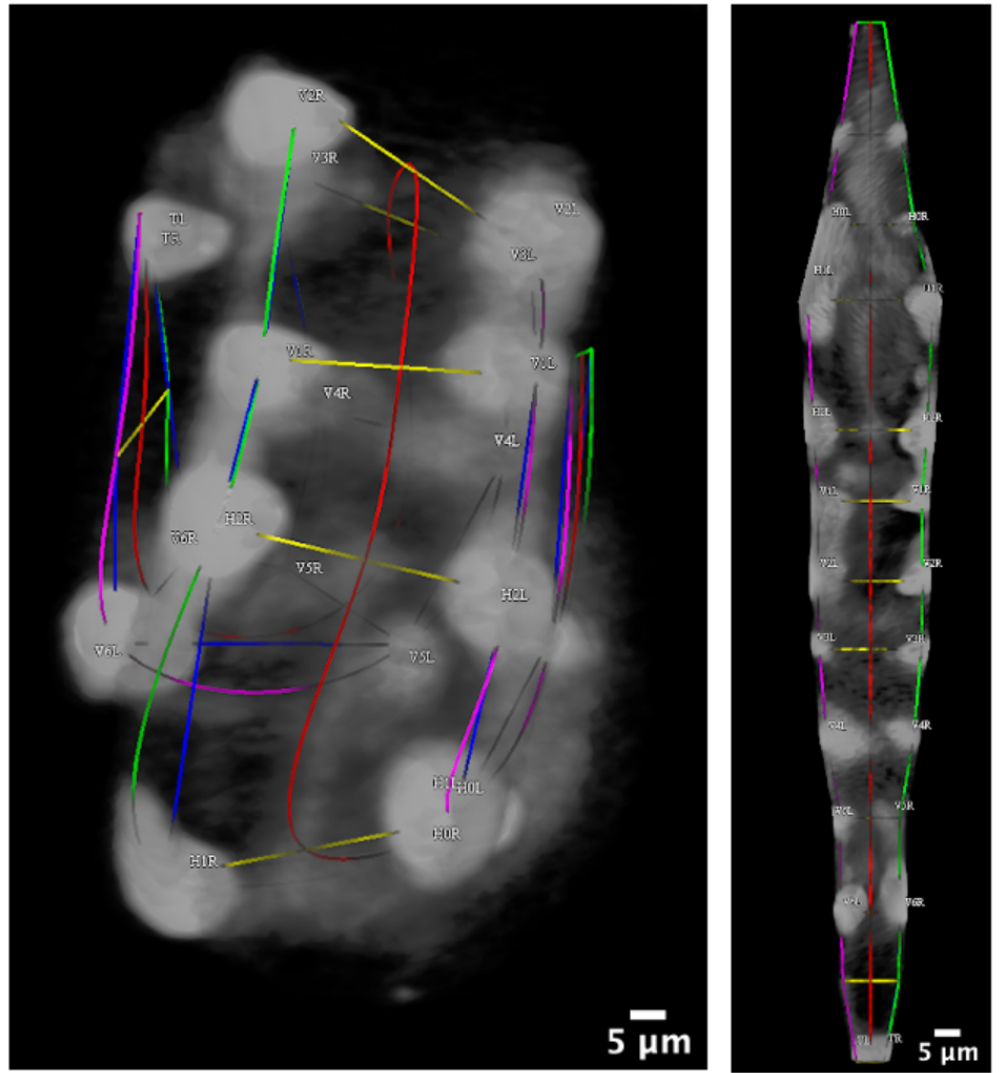


Fig 6. Rendered image volumes in the MIPAV GUI. The imaged twisted embryo (left) and imaged straightened embryo (right) rendered in Medical Image Processing, Analysis and Visualization (MIPAV) [12]. The fluorescent images are those depicted in Fig 1-A. Trained users navigate the MIPAV GUI to identify seam cells based upon relative positioning and other salient features such as specks of fluorescence on the skin. Green (left), red (center), and purple (right) splines yield an approximation of the coiled embryo's posture. Yellow lines connect seam cell nuclei laterally. The splines are used with the image volume to sweep planes orthogonal to the center spline, yielding the straightened embryo image.

will be referred to as *QAP*. Edge-wise (degree $d = 2$) features take the form of standardized chord lengths between nuclei. The first hypergraphical model, *Pairs*, employs a greater local context than *QAP* to describe relationships between seam cells. Hyperedges formed by two or three sequential pairs ($d = 4, 6$) better detail local regions throughout the embryo than is capable of a graphical model. Fig 7-A presents the hyperedge connectivity among nodes in the *Pairs* model [21]. The *Posture* model extends the *Pairs* model by leveraging complete posture ($d = n_1$) features in effort to

further discriminate between assignment hypotheses that appear similar in sequential regions of the embryo. Geometric features aim to contextualize the coiled embryo. Fig 8 illustrates three of the features used in the *Pairs* and *Posture* models. The angle Θ measures the angle between three successive pair midpoints. The angles Θ decrease throughout development as the worm elongates. Pair-to-pair twist angles ψ and τ penalizes assignments in which the posterior to anterior development is jagged and unnatural in appearance (SI-*C. elegans* Posture Modeling).

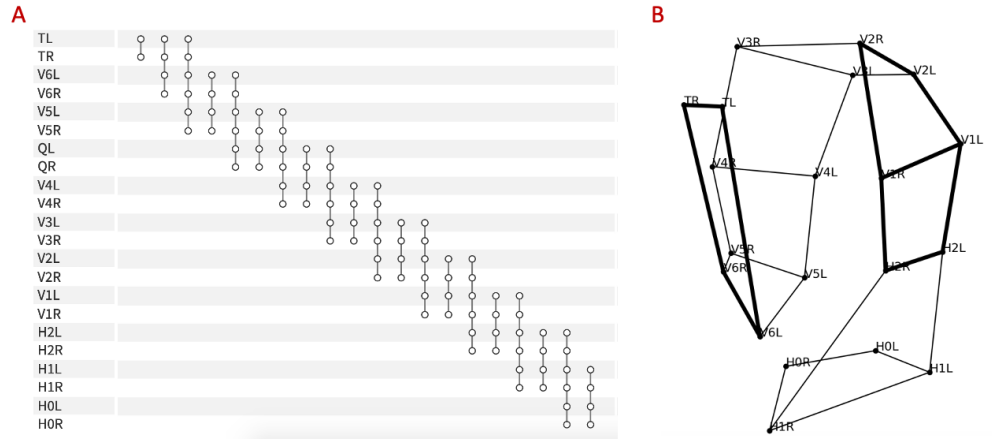


Fig 7. The *Pairs* hypergraphical model uses expansive local contexts about each portion of the embryo. A: The *Pairs* hyperedges connect local seam cell nuclei in sets of four and six. B: Degree four hyperedges connect sequential pairs of seam cells while degree six hyperedges connect sequential triplets of pairs. The posterior-most degree four hyperedge and a central degree six hyperedge are **bolded**.

Acknowledgments

Dr. Evan Ardiel was instrumental in developing descriptive features for identifying worm posture. Post-Baccalaureate research fellows Brandon Harvey and Nensi Karaj were supportive in providing data and discussions concerning the modeling. Dr. Zhen Zhang and Dr. Arye Nehorai provided assistance in using *KerGM* [2]. Dr. Vincent Lyzinski also provided insight on the methods. We also thank Dr. Hank Eden and Dr. Matthew Guay for their careful readings and suggestions. The code and data are available at <https://github.com/lauzier/EHGM>.

Supporting information

EHGM Pseudocode *EHGM* requires as input the branching step $k \in \{1, 2, \dots, n_1\}$, the dissimilarity tensors $\mathbf{Z}^{(d)}$, $d = 1, 2, \dots, n_1$, the size k permutation set \mathbf{P} , and optionally an initial upper bound C_0 on the global minimum C^* . The dissimilarity tensors are calculated given the reference hypergraph of size n_1 , either a previous frame hypergraph or a template hypergraph as described in section SI-Model Fitting. The n_2 input points and reference hypergraph are used to build the lower degree dissimilarity tensors $\mathbf{Z}^{(d)}$, $d \leq 2k$. The higher degree dissimilarity terms $d > 2k$ are calculated during

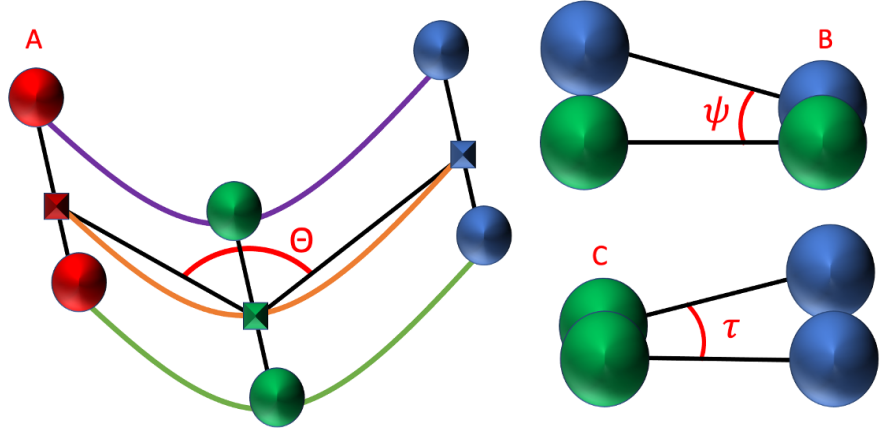


Fig 8. Hypergraphical geometric features contextualize seam cell assignments. Anatomically inspired geometric features describe bend and twist of a posture assignment. A: Three pairs of sequential nuclei: red, green, blue. Rectangles represent pair midpoints. The angle Θ in red is used as a degree six feature given six point to nuclei assignments. B, C: Degree four hypergraphical features measuring twist angles ψ and τ . These angles measure posterior to anterior twist pair-to-pair and left-right twist, respectively.

the search as required. Algorithm 1 initializes the search from the first candidate set $\mathbf{Q}_1 = \mathbf{P}$. The search is easily parallelized via initializing several first branches at a time. Each explores a disjoint section of \mathcal{X} .

Algorithm 1 initializes arrays and variables to start the recursive branch search (Algorithm 2). Eligible branch candidates are subset from the general queue \mathbf{P} into \mathbf{Q}_m via the *Enqueue* procedure (Algorithm 3). Each \mathbf{Q}_m contains the potential assignments for the next k terms that satisfy both the pruning constraints and assignment constraints specified by \mathcal{X} . The current assignment cost \tilde{C} is checked against the current minimum C^* upon reaching a complete assignment. The Backtrack procedure (Algorithm 4) removes \mathbf{k}_{m-1} from \mathbf{Q}_{m-1} when the path from \mathbf{k}_{m-1} is exhausted, which occurs when $\mathbf{Q}_m = \emptyset$. The recursion will continue until \mathbf{Q}_1 is empty, signaling the

complete enumeration of the search space S_n .

Algorithm 1: EHGM

Input: $k, C_0, \mathbf{P}, \mathbf{Z}^{(1)}, \dots, \mathbf{Z}^{(2k)}$
Output: $\mathbf{x}^*, C^* = f(\mathbf{x}^*)$
Initialization
 $C^* \leftarrow C_0$
 $\tilde{\mathbf{H}} = []$
 $\tilde{\mathbf{I}} = []$
 $\tilde{\mathbf{x}} \leftarrow \emptyset$
 $\tilde{C} \leftarrow 0$
 $m \leftarrow 1$
 $\mathbf{Q}_1 \leftarrow \text{Enqueue}(\tilde{\mathbf{x}}, \mathbf{P}, \tilde{C}, C^*, 1)$
while $\mathbf{Q}_1 \neq \emptyset$ **do**
 $\quad \mathbf{k}_1 \leftarrow \mathbf{Q}_1.pop()$
 $\quad \hat{H}_1 \leftarrow H_1(\mathbf{k}_1 | \mathbf{Z}^{(1)}, \dots, \mathbf{Z}^{(k)})$
 $\quad \tilde{C} \leftarrow \hat{H}_1$
 $\quad \tilde{\mathbf{H}}[1] = \hat{H}_1$
 $\quad \tilde{\mathbf{x}} \leftarrow \tilde{\mathbf{x}} \cup \{\mathbf{k}_1\}$
 $\quad m += 1$
 $\quad Visit(\mathbf{P}, \tilde{\mathbf{x}}, \tilde{C}, C^*, m)$
end
Return: \mathbf{x}^*, C^*

Algorithm 2: Visit

Input: $\mathbf{P}, \tilde{\mathbf{x}}, \tilde{C}, C^*, m$
 $\mathbf{Q}_m \leftarrow \text{Enqueue}(\tilde{\mathbf{x}}, \mathbf{P}, \tilde{C}, C^*, m)$
while $\mathbf{Q}_m \neq \emptyset$ **do**
 $\quad \hat{\mathbf{k}}_m \leftarrow \mathbf{Q}_m.pop()$
 $\quad \tilde{\mathbf{x}} \leftarrow \tilde{\mathbf{x}} \cup \{\hat{\mathbf{k}}_m\}$
 $\quad m += 1$
 $\quad \hat{H}_m \leftarrow H_m(\mathbf{k}_m | \tilde{\mathbf{x}}, \mathbf{Z}^{(1)}, \dots, \mathbf{Z}^{(2k)})$
 $\quad \tilde{\mathbf{H}}[m] = \hat{H}_m$
 $\quad \tilde{C} += \hat{H}_m$
if $m \geq 3$ **then**
 $\quad \hat{I}_m \leftarrow I_m(\mathbf{k}_m | \tilde{\mathbf{x}}, \mathbf{Z}^{(2k+1)}, \dots, \mathbf{Z}^{(mk)})$
 $\quad \tilde{\mathbf{I}}[m] = \hat{I}_m$
 $\quad \tilde{C} += \hat{I}_m$
end
if $m < M$ **then**
 $\quad Visit(\mathbf{P}, \tilde{\mathbf{x}}, \tilde{C}, C^*, m)$
else if $m = M$ **then**
 $\quad \text{if } \tilde{C} \leq C^* \text{ then}$
 $\quad \quad \mathbf{x}^* \leftarrow \tilde{\mathbf{x}}$
 $\quad \quad C^* \leftarrow \tilde{C}$
end
 $Backtrack(\tilde{\mathbf{x}}, \mathbf{Q}_{m-1}, m)$
end

Algorithm 3: Enqueue

Input: $\tilde{\mathbf{x}}, \mathbf{P}, \tilde{C}, C^*, m$
Output: \mathbf{Q}_m
 $\mathbf{Q}_m \leftarrow \emptyset$
for $\mathbf{k} \in \mathbf{P}$ **do**
| **if** $(\mathbf{k} \cap \tilde{\mathbf{x}} = \emptyset) \wedge (\tilde{C} + H_m(\mathbf{k}|\tilde{\mathbf{x}}) < C^*)$ **then**
| | $\mathbf{Q}_m \leftarrow \mathbf{Q}_m \cup \mathbf{k}$
| | **end**
| **end**

Algorithm 4: Backtrack

Input: $\tilde{\mathbf{x}}, \mathbf{Q}_{m-1}, m$
 $\mathbf{Q}_{m-1} \leftarrow \mathbf{Q}_{m-1} \setminus \tilde{\mathbf{x}}_m$
 $\tilde{\mathbf{x}} \leftarrow \{\hat{\mathbf{x}}_1, \hat{\mathbf{x}}_2, \dots, \hat{\mathbf{x}}_{m-1}\}$
 $\tilde{C} \leftarrow \sum_{j=1}^{m-1} (\mathbf{C}_m + \mathbf{I}_m)$

Hypergraphical Objective Decomposition The hypergraphical optimization objective can be decomposed according to hyperedge multiplicity and branching step. The stratification enables efficient search via **EHGM**.

Theorem 1. Assume an assignment problem objective f is in the form:

$$\begin{aligned} f(X|\mathbf{Z}^{(1)}, \mathbf{Z}^{(2)}, \dots, \mathbf{Z}^{(n_1)}) &= \sum_{l_1=1}^{n_1} \sum_{l'_1=1}^{n_2} \mathbf{Z}_{l_1 l'_1}^{(1)} x_{l_1 l'_1} + \sum_{l_1=1}^{n_1} \sum_{l'_1=1}^{n_2} \sum_{l_2=l_1+1}^{n_1} \sum_{l'_2=1}^{n_2} \mathbf{Z}_{l_1 l'_1 l_2 l'_2}^{(2)} x_{l_1 l'_1} x_{l_2 l'_2} \\ &+ \sum_{l_1=1}^{n_1} \sum_{l'_1=1}^{n_2} \sum_{l_2=l_1+1}^{n_1} \sum_{l'_2=1}^{n_2} \sum_{l_3=l_2+1}^{n_1} \sum_{l'_3=1}^{n_2} \mathbf{Z}_{l_1 l'_1 l_2 l'_2 l_3 l'_3}^{(3)} x_{l_1 l'_1} x_{l_2 l'_2} x_{l_3 l'_3} + \dots \\ &+ \sum_{l_1=1}^{n_1} \sum_{l'_1=1}^{n_2} \dots \sum_{l_{n_1}=l_{n_1-1}+1}^{n_1} \sum_{l'_{n_1}=1}^{n_2} \mathbf{Z}_{l_1 l'_1 \dots l_{n_1} l'_{n_1}}^{(n_1)} x_{l_1 l'_1} \dots x_{l_{n_1} l'_{n_1}} \end{aligned}$$

Then, for $k \in \{1, 2, \dots, n_1\}$, the stratification fully describes the objective f after $M = \frac{n_1}{k}$ branches. Define of H_1 , H_m , and I_m :

$$\begin{aligned} H_1(\mathbf{K}_1|\mathbf{Z}^{(1)}, \mathbf{Z}^{(2)}, \dots, \mathbf{Z}^{(k)}) &:= \\ \sum_{i_1=1}^k \mathbf{Z}_{l_{i_1} l'_{i_1}}^{(1)} + \sum_{i_1=1}^k \sum_{i_2=i_1+1}^k \mathbf{Z}_{l_{i_1} l'_{i_1} l_{i_2} l'_{i_2}}^{(2)} + \dots + \sum_{i_1=1}^k \sum_{i_2=i_1+1}^k \dots \sum_{i_k=i_{k-1}+1}^k \mathbf{Z}_{l_{i_1} l'_{i_1} l_{i_2} l'_{i_2} \dots l_{i_k} l'_{i_k}}^{(k)} & \end{aligned}$$

$$\begin{aligned} H_m(\mathbf{K}_m|\mathbf{K}_1, \dots, \mathbf{K}_{m-1}, \mathbf{Z}^{(1)}, \dots, \mathbf{Z}^{(2k)}) &:= \\ \sum_{i_1=(m-1)k+1}^{mk} \mathbf{Z}_{l_{i_1} l'_{i_1}}^{(1)} + \sum_{i_2=(m-1)k+1}^{mk} \sum_{i_1=1}^{i_2-1} \mathbf{Z}_{l_{i_1} l'_{i_1} l_{i_2} l'_{i_2}}^{(2)} & \\ + \sum_{i_3=(m-1)k+1}^{mk} \sum_{i_2=1}^{i_3-1} \sum_{i_1=1}^{i_2-1} \mathbf{Z}_{l_{i_1} l'_{i_1} l_{i_2} l'_{i_2} l_{i_3} l'_{i_3}}^{(3)} + \dots + \sum_{i_{2k}=(m-1)k+1}^{mk} \sum_{i_{2k-1}=1}^{i_{2k}-1} \dots \sum_{i_1=1}^{i_2-1} \mathbf{Z}_{l_{i_1} l'_{i_1} \dots l_{i_{2k}} l'_{i_{2k}}}^{(2k)} & \end{aligned}$$

$$I_m(\mathbf{K}_m | \mathbf{K}_1, \mathbf{K}_2, \dots, \mathbf{K}_{m-1}, \mathbf{Z}^{(2k+1)}, \dots, \mathbf{Z}^{(mk)}) := \sum_{d=2k+1}^{mk} \Xi_m^{(d)}$$

where

$$\Xi_m^{(d)}(\mathbf{K}_m | \mathbf{K}_1, \mathbf{K}_2, \dots, \mathbf{K}_{m-1}, \mathbf{Z}^{(2k+1)}, \dots, \mathbf{Z}^{(mk)}) := \sum_{i_d=(m-1)k+1}^{mk} \sum_{i_{d-1}=1}^{i_d-1} \dots \sum_{i_1=1}^{i_2-1} \mathbf{Z}_{l_{i_1} l'_{i_1} \dots l_{i_d} l'_{i_d}}^{(d)}$$

Then, the degree n_1 hypergraph matching objective f can be expressed

$$f(X | \mathbf{Z}^{(1)}, \mathbf{Z}^{(2)}, \dots, \mathbf{Z}^{(n_1)}) = \sum_{m=1}^m H_m + \sum_{m=3}^m I_m$$

Proof. First consider the single branching case $k = 1$. This yields $M = \frac{n_1}{k} = \frac{n_1}{1} = n_1$ branches. Each branch yields one assignment; i.e. $K_m = l'_m$ is assigned to vertex l_m . The initial branch selection rule H_1 can only utilize the first order term:

$$H_1(K_1 | \mathbf{Z}^{(1)}) = \mathbf{Z}_{l_1 l'_1}^{(1)}$$

Then the general selection rule for the second branch will: gather the first order costs for the second assignment as well as the quadratic (second order) costs between the first two assignments:

$$H_2(K_2 | K_1, \mathbf{Z}^{(1)}, \mathbf{Z}^{(2)}) = \mathbf{Z}_{l_2 l'_2}^{(1)} + \sum_{i_2=2}^2 \sum_{i_1=1}^{i_2-1} \mathbf{Z}_{l_{i_1} l'_{i_1} l_{i_2} l'_{i_2}}^{(2)} = \mathbf{Z}_{l_2}^{(1)} + \mathbf{Z}_{l_1 l'_1 l_2 l'_2}^{(2)}$$

The third branching step will include H_3 and I_3 . H_3 follows from H_2 :

$$H_3(K_3 | K_1, K_2, \mathbf{Z}^{(1)}, \mathbf{Z}^{(2)}) = \mathbf{Z}_{l_3 l'_3}^{(1)} + \sum_{i_2=3}^3 \sum_{i_1=1}^{i_2-1} \mathbf{Z}_{l_{i_1} l'_{i_1} l_{i_2} l'_{i_2}}^{(2)} = \mathbf{Z}_{l_3}^{(1)} + \mathbf{Z}_{l_1 l'_1 l_3 l'_3}^{(2)} + \mathbf{Z}_{l_2 l'_2 l_3 l'_3}^{(2)}$$

$$I_3(K_3 | K_1, K_2, \mathbf{Z}^{(3)}) = \Xi_m^{(3)} = \mathbf{Z}_{l_1 l'_1 l_2 l'_2 l_3 l'_3}^{(3)}$$

Note that if $n_1 = 3$, then $H_1 + H_2 + H_3 + I_3$ fully describes the third order assignment problem:

$$\begin{aligned} H_1 + H_2 + H_3 + I_3 &= \underbrace{\mathbf{Z}_{l_1 l'_1}^{(1)}}_{H_1} + \underbrace{\mathbf{Z}_{l_2 l'_2}^{(1)} + \mathbf{Z}_{l_1 l'_1 l_2 l'_2}^{(2)}}_{H_2} + \underbrace{\mathbf{Z}_{l_3 l'_3}^{(1)} + \mathbf{Z}_{l_1 l'_1 l_3 l'_3}^{(2)} + \mathbf{Z}_{l_2 l'_2 l_3 l'_3}^{(2)}}_{H_3} + \underbrace{\mathbf{Z}_{l_1 l'_1 l_2 l'_2 l_3 l'_3}^{(3)}}_{I_3} \\ &= \sum_{i_1=1}^3 \mathbf{Z}_{l_{i_1} l'_{i_1}}^{(1)} + \sum_{i_1=1}^3 \sum_{i_2=i_1+1}^3 \mathbf{Z}_{l_{i_1} l'_{i_1} l_{i_2} l'_{i_2}}^{(2)} + \sum_{i_1=1}^3 \sum_{i_2=i_1+1}^3 \sum_{i_3=i_2+1}^3 \mathbf{Z}_{l_{i_1} l'_{i_1} l_{i_2} l'_{i_2} l_{i_3} l'_{i_3}}^{(3)} \\ &= f(X | \mathbf{Z}^{(1)}, \mathbf{Z}^{(2)}, \mathbf{Z}^{(3)}) \quad (7) \end{aligned}$$

Now consider the extension to $n_1 = 4$, yielding a fourth degree assignment problem. The fourth branch will assign the next term, $K_4 = l'_4$. The terms H_4 and I_4 will then fully specify the fourth degree problem:

$$H_4(K_4|K_1, K_2, K_3, \mathbf{Z}^{(1)}, \mathbf{Z}^{(2)}) = \mathbf{Z}_{l_4 l'_4}^{(1)} + \mathbf{Z}_{l_1 l'_1 l_4 l'_4}^{(2)} + \mathbf{Z}_{l_2 l'_2 l_4 l'_4}^{(2)} + \mathbf{Z}_{l_3 l'_3 l_4 l'_4}^{(2)}$$

The second aggregation rule I_4 will consider third order terms between branches 1, 2 and 4 as well as the fourth order term using all four assignments:

$$I_4(K_4|K_1, K_2, K_3, \mathbf{Z}^{(3)}, \mathbf{Z}^{(4)}) = \Xi_4^{(3)} + \Xi_4^{(4)} = \mathbf{Z}_{l_1 l'_1 l_2 l'_2 l_4 l'_4}^{(3)} + \mathbf{Z}_{l_2 l'_2 l_3 l'_3 l_4 l'_4}^{(3)} + \mathbf{Z}_{l_1 l'_1 l_2 l'_2 l_3 l'_3 l_4 l'_4}^{(4)}$$

Joining the fourth branch:

$$\begin{aligned} H_1 + H_2 + H_3 + I_3 + H_4 + I_4 &= \\ &\underbrace{\sum_{i_1=1}^3 \mathbf{Z}_{l_{i_1} l'_{i_1}}^{(1)} + \sum_{i_1=1}^3 \sum_{i_2=i_1+1}^3 \mathbf{Z}_{l_{i_1} l'_{i_1} l_{i_2} l'_{i_2}}^{(2)} + \sum_{i_1=1}^3 \sum_{i_2=i_1+1}^3 \sum_{i_3=i_2+1}^3 \mathbf{Z}_{l_{i_1} l'_{i_1} l_{i_2} l'_{i_2} l_{i_3} l'_{i_3}}^{(3)}}_{H_1 + H_2 + H_3 + I_3} \\ &+ \underbrace{\mathbf{Z}_{l_4 l'_4}^{(1)} + \mathbf{Z}_{l_1 l'_1 l_4 l'_4}^{(2)} + \mathbf{Z}_{l_2 l'_2 l_4 l'_4}^{(2)} + \mathbf{Z}_{l_3 l'_3 l_4 l'_4}^{(2)} + \mathbf{Z}_{l_1 l'_1 l_2 l'_2 l_4 l'_4}^{(3)} + \mathbf{Z}_{l_2 l'_2 l_3 l'_3 l_4 l'_4}^{(3)} + \mathbf{Z}_{l_1 l'_1 l_2 l'_2 l_3 l'_3 l_4 l'_4}^{(4)}}_{H_4} \\ &= \sum_{i_1=1}^4 \mathbf{Z}_{l_{i_1} l'_{i_1}}^{(1)} + \sum_{i_1=1}^4 \sum_{i_2=i_1+1}^4 \mathbf{Z}_{l_{i_1} l'_{i_1} l_{i_2} l'_{i_2}}^{(2)} + \sum_{i_1=1}^4 \sum_{i_2=i_1+1}^4 \sum_{i_3=i_2+1}^4 \mathbf{Z}_{l_{i_1} l'_{i_1} l_{i_2} l'_{i_2} l_{i_3} l'_{i_3}}^{(3)} \\ &+ \sum_{i_1=1}^4 \sum_{i_2=i_1+1}^4 \sum_{i_3=i_2+1}^4 \sum_{i_4=i_3+1}^4 \mathbf{Z}_{l_{i_1} l'_{i_1} l_{i_2} l'_{i_2} l_{i_3} l'_{i_3} l_{i_4} l'_{i_4}}^{(4)} \\ &= f(X|\mathbf{Z}^{(1)}, \mathbf{Z}^{(2)}, \mathbf{Z}^{(3)}, \mathbf{Z}^{(4)}) \quad (8) \end{aligned}$$

Now consider the arbitrary $(m+1)^{st}$ branch. This will yield the full objective for an assignment problem of size $m+1$ up to degree $m+1$.

$$\begin{aligned} \sum_{p=1}^{m+1} H_p + \sum_{p=3}^{m+1} I_p &= \sum_{p=1}^m H_p + \sum_{p=3}^m I_p + H_{m+1} + I_{m+1} = \\ &\underbrace{\sum_{i_1=1}^m \mathbf{Z}_{l_{i_1} l'_{i_1}}^{(1)} + \sum_{i_1=1}^m \sum_{i_2=i_1+1}^m \mathbf{Z}_{l_{i_1} l'_{i_1} l_{i_2} l'_{i_2}}^{(2)} + \cdots + \sum_{i_1=1}^m \sum_{i_2=i_1+1}^m \cdots \sum_{i_m=i_{m-1}+1}^m \mathbf{Z}_{l_{i_1} l'_{i_1} l_{i_2} l'_{i_2} \cdots l_{i_m} l'_{i_m}}^{(m)}}_{\sum_{p=1}^m H_p + \sum_{p=3}^m I_p} \\ &+ \underbrace{\mathbf{Z}_{l_{i_{m+1}} l'_{i_{m+1}}}^{(1)} + \sum_{i_1=1}^m \mathbf{Z}_{l_{i_1} l'_{i_1} l_{i_{m+1}} l'_{i_{m+1}}}^{(2)} + \cdots + \sum_{d=3}^{m+1} \Xi_{m+1}^{(d)}}_{H_{m+1}} \quad (9) \end{aligned}$$

It is sufficient to show each degree $d \in \{1, 2, \dots, m+1\}$ hyperedge is fully accounted for across all $m+1$ points to prove the $(m+1)^{st}$ branch satisfies the objective f . The hyperedge costs across all points will be decomposed into three disjoint sets, and each set considered at a time:

$$\{1\}, \{2\}, \{3, \dots, m\}, \{m+1\}$$

The first and final of the four cases are trivial. The first degree terms are enumerated via the first term in H_{m+1} , while $X i_{m+1}^{(m+1)}$ explicitly addresses the degree $m+1$ hyperedge comprising all assignments: $\mathbf{Z}_{l_1 l'_1 l_2 l'_2 \dots l_{m+1} l'_{m+1}}^{(m+1)}$. We will focus on the second and third cases. The degree $d=2$ terms are formed by the addition of branch $m+1$ are considered in term H_{m+1} :

$$\sum_{i_1=1}^m \sum_{i_2=i_1+1}^m \mathbf{Z}_{l_{i_1} l'_{i_1} l_{i_2} l'_{i_2}}^{(2)} + \sum_{i_1=1}^m \mathbf{Z}_{l_{i_1} l'_{i_1} l_{i_{m+1}} l'_{i_{m+1}}}^{(2)} = \sum_{i_1=1}^{m+1} \sum_{i_2=i_1+1}^{m+1} \mathbf{Z}_{l_{i_1} l'_{i_1} l_{i_2} l'_{i_2}}^{(2)}$$

Let $d \in \{3, \dots, m\}$. The completion is similar to the $d=2$ degree case; however, the term $\Xi_{m+1}^{(d)}$ in I_{m+1} address higher degree hyperedges up to and including degree m concerning branch $m+1$:

$$\sum_{i_1=1}^m \dots \sum_{i_d=i_{d-1}+1}^m \mathbf{Z}_{l_{i_1} l'_{i_1} \dots l_{i_d} l'_{i_d}}^{(d)} + \Xi_{m+1}^{(d)} = \sum_{i_1=1}^{m+1} \dots \sum_{i_d=i_{d-1}+1}^{m+1} \mathbf{Z}_{l_{i_1} l'_{i_1} \dots l_{i_d} l'_{i_d}}^{(d)}$$

Therefore, the $(m+1)^{st}$ step fully accrues the objective f :

$$\sum_{p=1}^{m+1} H_p + \sum_{p=3}^{m+1} I_p = f(X | \mathbf{Z}^{(1)}, \mathbf{Z}^{(2)}, \dots, \mathbf{Z}^{(m+1)})$$

Then inductively, the stratification holds such that:

$$\sum_{m=1}^{n_1} H_m + \sum_{m=3}^{n_1} I_m = f(X | \mathbf{Z}^{(1)}, \mathbf{Z}^{(2)}, \dots, \mathbf{Z}^{(n_1)})$$

Now consider the plural branching rule $k > 1$. The proof will follow from the single assignment branching case. The base case at the fourth branch will be established, followed by the induction hypothesis demonstrating the branching from m to $m+1$. First, define the terms H_1, H_2, H_3, I_3, H_4 , and I_4 :

$$H_1 = \sum_{i_1=1}^k \mathbf{Z}_{l_{i_1} l'_{i_1}}^{(1)} + \sum_{i_1=1}^k \sum_{i_2=i_1+1}^k \mathbf{Z}_{l_{i_1} l'_{i_1} l_{i_2} l'_{i_2}}^{(2)} + \dots + \sum_{i_1=1}^k \sum_{i_2=i_1+1}^k \dots \sum_{i_k=i_{k-1}+1}^k \mathbf{Z}_{l_{i_1} l'_{i_1} l_{i_2} l'_{i_2} \dots l_{i_k} l'_{i_k}}^{(k)} \quad (10)$$

$$H_2 = \sum_{i_1=k+1}^{2k} \mathbf{Z}_{l_{i_1} l'_{i_1}}^{(1)} + \sum_{i_2=k+1}^{2k} \sum_{i_1=1}^{i_2-1} \mathbf{Z}_{l_{i_1} l'_{i_1} l_{i_2} l'_{i_2}}^{(2)} + \dots + \sum_{i_{2k}=k+1}^{2k} \dots \sum_{i_2=1}^{i_3-1} \sum_{i_1=1}^{i_2-1} \mathbf{Z}_{l_{i_1} l'_{i_1} \dots l_{i_{2k}} l'_{i_{2k}}}^{(2k)} \quad (11)$$

$$H_3 = \sum_{i_1=2k+1}^{3k} \mathbf{Z}_{l_{i_1} l'_{i_1}}^{(1)} + \sum_{i_2=2k+1}^{3k} \sum_{i_1=1}^{i_2-1} \mathbf{Z}_{l_{i_1} l'_{i_1} l_{i_2} l'_{i_2}}^{(2)} + \dots + \sum_{i_{2k}=2k+1}^{3k} \dots \sum_{i_1=1}^{i_2-1} \mathbf{Z}_{l_{i_1} l'_{i_1} \dots l_{i_{2k}} l'_{i_{2k}}}^{(2k)} \quad (12)$$

$$I_3 = \sum_{d=2k+1}^{3k} \Xi_3^{(d)} \quad (13)$$

$$H_4 = \sum_{i_1=3k+1}^{4k} \mathbf{Z}_{l_{i_1} l'_{i_1}}^{(1)} + \sum_{i_2=3k+1}^{4k} \sum_{i_1=1}^{i_2-1} \mathbf{Z}_{l_{i_1} l'_{i_1} l_{i_2} l'_{i_2}}^{(2)} + \dots + \sum_{i_{2k}=3k+1}^{4k} \dots \sum_{i_1=1}^{i_2-1} \mathbf{Z}_{l_{i_1} l'_{i_1} \dots l_{i_{2k}} l'_{i_{2k}}}^{(2k)} \quad (14)$$

$$I_4 = \sum_{d=3k+1}^{4k} \Xi_4^{(d)} \quad (15)$$

The terms presented thus far for the general $k > 1$ case fully describe all terms concerning assignments $1, 2, \dots, 4k$ up to degree $4k$. The hyperedge multiplicities will again be partitioned into disjoint groups:

$$\{1\}, \{2, \dots, k\}, \{k+1, \dots, 2k\}, \{2k+1, \dots, 3k\}, \{3k+1, \dots, 4k\}$$

The first case is trivial, just as in the single assignment branching ($k = 1$) proof. Unary terms are accounted for in the first summand of each H_m . Then, consider $d \in \{2, \dots, k\}$:

$$\begin{aligned} & \underbrace{\sum_{i_1=1}^k \dots \sum_{i_d=i_{d-1}+1}^k \mathbf{Z}_{l_{i_1} l'_{i_1} \dots l_{i_d} l'_{i_d}}^{(d)}}_{H_1} + \underbrace{\sum_{i_d=k+1}^{2k} \sum_{i_{d-1}=1}^{i_d-1} \dots \sum_{i_1=1}^{i_2-1} \mathbf{Z}_{l_{i_1} l'_{i_1} \dots l_{i_d} l'_{i_d}}^{(d)}}_{H_2} \\ & + \underbrace{\sum_{i_d=2k+1}^{3k} \sum_{i_{d-1}=1}^{i_d-1} \dots \sum_{i_1=1}^{i_2-1} \mathbf{Z}_{l_{i_1} l'_{i_1} \dots l_{i_d} l'_{i_d}}^{(d)}}_{H_3} + \underbrace{\sum_{i_d=3k+1}^{4k} \sum_{i_{d-1}=1}^{i_d-1} \dots \sum_{i_1=1}^{i_2-1} \mathbf{Z}_{l_{i_1} l'_{i_1} \dots l_{i_d} l'_{i_d}}^{(d)}}_{H_4} \\ & = \sum_{i_1=1}^{4k} \sum_{i_2=i_1+1}^{4k} \dots \sum_{i_d=i_{d-1}+1}^{4k} \mathbf{Z}_{l_{i_1} l'_{i_1} \dots l_{i_d} l'_{i_d}}^{(d)} \end{aligned}$$

The proof for degree $d \in \{k+1, \dots, 2k\}$ follows immediately from the grouping presented above, but without the initial branch selection rule term H_1 . Next, assume $d \in \{2k+1, \dots, (m-1)k\}$. Degree d hyperedge dissimilarities will be contained in both I_3 and I_4 terms:

$$\begin{aligned} & \underbrace{\sum_{i_d=2k+1}^{3k} \sum_{i_{d-1}=1}^{i_d-1} \dots \sum_{i_1=1}^{i_2-1} \mathbf{Z}_{l_{i_1} l'_{i_1} \dots l_{i_d} l'_{i_d}}^{(d)}}_{I_3} + \underbrace{\sum_{i_d=3k+1}^{4k} \sum_{i_{d-1}=1}^{i_d-1} \dots \sum_{i_1=1}^{i_2-1} \mathbf{Z}_{l_{i_1} l'_{i_1} \dots l_{i_d} l'_{i_d}}^{(d)}}_{I_4} \\ & = \sum_{i_1=1}^{4k} \dots \sum_{i_{d-1}=i_{d-2}+1}^{4k} \sum_{i_d=i_{d-1}+1}^{4k} \mathbf{Z}_{l_{i_1} l'_{i_1} \dots l_{i_d} l'_{i_d}}^{(d)} \end{aligned}$$

Since $d \leq 2k+1$, the terms only appear in the third branch term I_3 when the assignment $2k+1$ is committed. The final set arises from the definition of I_4 which accrues hyperedges of degree $d \in \{3k+1, \dots, 4k\}$ across assignments in branches $m = 1, 2, 3, 4$. The base case is fully established for the arbitrary $k > 1$ case. The final step of the proof is to establish the extension of the $(m+1)^{st}$ branch:

$$\begin{aligned}
\sum_{p=1}^{m+1} H_p + \sum_{p=3}^{m+1} I_p &= \sum_{p=1}^m H_p + \sum_{p=3}^m I_p + H_{m+1} + I_{m+1} = \\
&\underbrace{\sum_{i_1=1}^{mk} \mathbf{Z}_{l_{i_1} l'_{i_1}}^{(1)} + \sum_{i_1=1}^{mk} \sum_{i_2=i_1+1}^{mk} \mathbf{Z}_{l_{i_1} l'_{i_1} l_{i_2} l'_{i_2}}^{(2)} + \cdots + \sum_{i_1=1}^{mk} \sum_{i_2=i_1+1}^{mk} \cdots \sum_{i_{mk}=i_{mk-1}+1}^{mk} \mathbf{Z}_{l_{i_1} l'_{i_1} \cdots l_{i_{mk}} l'_{i_{mk}}}^{(mk)}}_{\sum_{p=1}^m H_p + \sum_{p=3}^m I_p} \\
&+ \underbrace{\sum_{i_1=mk+1}^{(m+1)k} \mathbf{Z}_{l_{i_1} l'_{i_1}}^{(1)} + \cdots + \sum_{i_{2k}=mk+1}^{(m+1)k} \sum_{i_{2k-1}=1}^{i_{2k}-1} \cdots \sum_{i_1=1}^{i_2-1} \mathbf{Z}_{l_{i_1} l'_{i_1} \cdots l_{i_{2k}} l'_{i_{2k}}}^{(2k)}}_{H_{m+1}} + \underbrace{\sum_{d=2k+1}^{(m+1)k} \Xi_{m+1}^{(d)}}_{I_{m+1}} \quad (16)
\end{aligned}$$

The $(m+1)k$ hyperedge multiplicities will be stratified into four groups:

$$\{1\}, \{2, \dots, 2k\}, \{2k+1, \dots, mk\}, \{mk+1, \dots, (m+1)k\}$$

Just as in the singular $k=1$ case, the proof for the first and last groups are trivial. The unary terms are again evident from the first term in H_{m+1} , while the $mk+1 \leq d \leq (m+1)k$ terms in I_{m+1} fully encapsulates the fourth group. The steps in the remaining two cases will follow that of the $k=1$ case.

First, assume $d \in \{2, \dots, 2k\}$. The extension of the $(m+1)^{st}$ branch uses exclusively the selection rule H_{m+1} :

$$\begin{aligned}
&\underbrace{\sum_{i_1=1}^{mk} \cdots \sum_{i_{d-1}=i_{d-2}+1}^{mk} \sum_{i_d=i_{d-1}+1}^{mk} \mathbf{Z}_{l_{i_1} l'_{i_1} \cdots l_{i_d} l'_{i_d}}^{(d)}}_{\sum_{p=1}^m H_p} + \underbrace{\sum_{i_d=mk+1}^{(m+1)k} \sum_{i_{d-1}=1}^{i_d-1} \cdots \sum_{i_1=1}^{i_2-1} \mathbf{Z}_{l_{i_1} l'_{i_1} \cdots l_{i_d} l'_{i_d}}^{(d)}}_{H_{m+1}} = \\
&\sum_{i_1=1}^{(m+1)k} \cdots \sum_{i_{d-1}=i_{d-2}+1}^{(m+1)k} \sum_{i_d=i_{d-1}+1}^{(m+1)k} \mathbf{Z}_{l_{i_1} l'_{i_1} \cdots l_{i_d} l'_{i_d}}^{(d)} \quad (17)
\end{aligned}$$

Next, assume $d \in \{2k+1, \dots, mk\}$. These terms are captured in I_{m+1} using each definition of $\Xi_{m+1}^{(d)}$:

$$\begin{aligned}
&\underbrace{\sum_{i_1=1}^{mk} \cdots \sum_{i_{d-1}=i_{d-2}+1}^{mk} \sum_{i_d=i_{d-1}+1}^{mk} \mathbf{Z}_{l_{i_1} l'_{i_1} \cdots l_{i_d} l'_{i_d}}^{(d)}}_{I_{m+1}} + \underbrace{\sum_{i_d=mk+1}^{(m+1)k} \sum_{i_{d-1}=1}^{i_d-1} \cdots \sum_{i_1=1}^{i_2-1} \mathbf{Z}_{l_{i_1} l'_{i_1} \cdots l_{i_d} l'_{i_d}}^{(d)}}_{I_{m+1}} = \\
&\sum_{i_1=1}^{(m+1)k} \cdots \sum_{i_{d-1}=i_{d-2}+1}^{(m+1)k} \sum_{i_d=i_{d-1}+1}^{(m+1)k} \mathbf{Z}_{l_{i_1} l'_{i_1} \cdots l_{i_d} l'_{i_d}}^{(d)} \quad (18)
\end{aligned}$$

All four results together show that every degree hyperedge $1, \dots, (m+1)k$ is accounted for in the $(m+1)^{st}$ branch, thus proving the induction hypothesis:

$$\sum_{p=1}^{m+1} H_p + \sum_{p=3}^{m+1} I_p = f(X | \mathbf{Z}^{(1)}, \mathbf{Z}^{(2)}, \dots, \mathbf{Z}^{((m+1)k)})$$

The M^{th} branch completes the degree n_1 assignment problem of size n_1 . For any $k \in \{1, 2, \dots, n_1\}$, the selection and aggregation rules yield the full degree n_1 assignment problem objective:

$$\sum_{p=1}^M H_p + \sum_{p=3}^M I_p = f(X | \mathbf{Z}^{(1)}, \mathbf{Z}^{(2)}, \dots, \mathbf{Z}^{(n_1)})$$

□

Convergence & Exactness of **EHGM**

Theorem 2. *EHGM (algorithm 1) will converge to a globally optimal solution of the following hypergraph matching optimization problem given input $k \in \{1, 2, \dots, n_1\}$:*

$$\begin{aligned} \min_{X \in \mathcal{X}} \sum_{l_1=1}^{n_1} \sum_{l'_1=1}^{n_2} \mathbf{Z}_{l_1 l'_1}^{(1)} x_{l_1 l'_1} &+ \sum_{l_1=1}^{n_1} \sum_{l'_1=1}^{n_2} \sum_{l_2=l_1+1}^{n_1} \sum_{l'_2=1}^{n_2} \mathbf{Z}_{l_1 l'_1 l_2 l'_2}^{(2)} x_{l_1 l'_1} x_{l_2 l'_2} \\ &+ \sum_{l_1=1}^{n_1} \sum_{l'_1=1}^{n_2} \sum_{l_2=l_1+1}^{n_1} \sum_{l'_2=1}^{n_2} \sum_{l_3=l_2+1}^{n_1} \sum_{l'_3=1}^{n_2} \mathbf{Z}_{l_1 l'_1 l_2 l'_2 l_3 l'_3}^{(3)} x_{l_1 l'_1} x_{l_2 l'_2} x_{l_3 l'_3} + \dots \\ &+ \sum_{l_1=1}^{n_1} \sum_{l'_1=1}^{n_2} \dots \sum_{l_{n_1}=l_{n_1-1}+1}^{n_1} \sum_{l'_{n_1}=1}^{n_2} \mathbf{Z}_{l_1 l'_1 \dots l_{n_1} l'_{n_1}}^{(n_1)} x_{l_1 l'_1} \dots x_{l_{n_1} l'_{n_1}} \end{aligned} \quad (19)$$

where \mathcal{X} is defined:

$$\mathcal{X} = \{X \in \{0, 1\}^{n_1 \times n_2} : \forall j, \sum_{i=1}^{n_1} x_{l_i l'_j} = 1, \forall i, \sum_{j=1}^{n_2} x_{l_i l'_j} \leq 1\}$$

Proof. First, we will show **EHGM** converges, then it will be proven that the converged solution is globally optimal.

The search begins with initializing queue $\mathbf{Q}_1 = \mathbf{P}$. The algorithm terminates with the exhaustion of \mathbf{Q}_1 . Each set $\mathbf{Q}_m \subset \mathbf{P}$ contains feasible k -assignments conditioned on the assignment constraints and costs \tilde{C}, C^* . *Backtrack* (Algorithm 4) removes \mathbf{x}_m from \mathbf{Q}_{m-1} upon enumeration of \mathbf{Q}_m . The recursion then falls back to selecting from branch $m-1$, eventually exhausting \mathbf{Q}_{m-1} just as in the enumeration of \mathbf{Q}_m . This recursion continues until the first branch $\mathbf{k}_1 \in \mathbf{Q}_1$ is removed, signaling the exploration of all assignments originating with the k -tuple \mathbf{k}_1 . The exploration is repeated for each $\mathbf{k}_1 \in \mathbf{Q}_1$. Thus, all possible assignments $X \in \mathcal{X}$ are explored via the branching scheme.

Assignments accrue a monotonically increasing cost \tilde{C} to be compared to C^* with accompanying assignment \mathbf{x}^* at each branch. A complete assignment then drops the last k assignments from $\tilde{\mathbf{x}}$, initializing the backwards recursion, emptying \mathbf{Q}_m until $\mathbf{k}_{m-1}^{(n_k)} \in \mathbf{Q}_{m-1}$ is exhausted. There are at most $|\mathbf{Q}_m| \leq n_k$ viable permutations at branch m . Each possible branch is evaluated from $\tilde{\mathbf{x}} = [\mathbf{k}_1, \mathbf{k}_2, \dots, \mathbf{k}_{m-1}]$. The $(m-1)^{st}$ branch $\mathbf{k}_{m-1} \in \mathbf{Q}_{m-1}$ is removed from \mathbf{Q}_{m-1} upon exhaustion of \mathbf{Q}_m :

$$\begin{aligned} \tilde{\mathbf{x}}_1^{(m)} &= [\mathbf{k}_1^{(1)}, \mathbf{k}_2^{(1)}, \dots, \mathbf{k}_{m-1}^{(1)}, \mathbf{k}_m^{(1)}] \\ \tilde{\mathbf{x}}_2^{(m)} &= [\mathbf{k}_1^{(1)}, \mathbf{k}_2^{(1)}, \dots, \mathbf{k}_{m-1}^{(1)}, \mathbf{k}_m^{(2)}] \\ &\dots \\ \tilde{\mathbf{x}}_{n_k}^{(m)} &= [\mathbf{k}_1^{(1)}, \mathbf{k}_2^{(1)}, \dots, \mathbf{k}_{m-1}^{(1)}, \mathbf{k}_m^{(n_k)}] \end{aligned}$$

Each of the n_k possible final branches from $\mathbf{k}_{m-1}^{(1)}$ is explored, then $\mathbf{k}_{m-1}^{(1)}$ is removed from \mathbf{Q}_{m-1} .

The process follows for the M^{th} branch, exhausting viable assignment sets until \mathbf{k}_{M-1} is removed. The recursion follows inductively back to the exhaustion of \mathbf{Q}_1 , signaling the end of the search. Thus, all possible assignments $X \in \mathcal{X}$ are explored via the branching scheme.

The convergent and exhaustive algorithm will yield a globally optimal solution $C^* = f(\mathbf{x}^*)$ after exhausting \mathbf{Q}_1 . As proven above the additive decomposition of the cost structure (equation 2) is proven to be satisfied by summing all selection and aggregation rule terms. Assume an uninformed initialization $C^* = \infty$. Then the first pass will greedily take the best permutation from the first set \mathbf{Q}_1 : $\mathbf{k}_1^{(1)}$, and the best from the second set given it does not conflict with $\mathbf{k}_1^{(1)}$: $\mathbf{k}_2^{(2|1)}$. This process will continue until the first complete assignment:

$\tilde{\mathbf{x}} = [\mathbf{k}_1^{(1)}, \mathbf{k}_2^{(2|1)}, \mathbf{k}_3^{(3|2,1)}, \dots, \mathbf{k}_M^{(M|(M-1), \dots, 1)}]$ with $\tilde{C} = f(\tilde{\mathbf{x}})$. The first *Bracktrack* removes $\mathbf{k}_M^{(M|(M-1), \dots, 1)}$, and the M^{th} *Visit* call will exhaust \mathbf{Q}_M . Subsequent *Enqueue* calls will limit only allow branches that satisfy both the assignment constraints and the updated selection rule cost (Algorithm 3). This follows that any k -tuple of assignments $\mathbf{k}_m^{(j)}$ such that for $\tilde{\mathbf{x}} = [\mathbf{k}_1^{(j_1)}, \mathbf{k}_2^{(j_2|j_1)}, \dots, \mathbf{k}_m^{(j_d|j_{(m-1)}, \dots, j_1)}]$:

$$\tilde{C} + H_m(\tilde{\mathbf{x}}_{m-1}, \mathbf{k}_m^{(j_d|j_{(m-1)}, \dots, j_1)}) < C^*$$

The additive decomposition of the objective paired with the assumed non-negativity of the dissimilarity tensors $\mathbf{Z}^{(j)}$ results in each branch monotonically increasing \tilde{C} :

$$\tilde{C} + H_m(\tilde{\mathbf{x}}_{m-1}, \mathbf{k}_m^{(j_d|j_{(m-1)}, \dots, j_1)}) + I_m(\mathbf{k}_1^{(j_1)}, \mathbf{k}_2^{(j_2|j_1)}, \dots, \mathbf{k}_m^{(j_d|j_{(m-1)}, \dots, j_1)}) \geq \tilde{C}$$

The convergent search will thus eliminate all paths that are not globally optimal. Incrementally updating the reserved solution \mathbf{x}^* with cost C^* expedites convergence as each replacement is necessarily a better solution. The resulting \mathbf{x}^* and corresponding cost C^* are such that at no other full assignment $\tilde{\mathbf{x}}$ can replace \mathbf{x}^* , by definition a globally optimal solution of f .

□

Model Fitting Expert annotations are used to derive features such that the correct assignment consistently achieves a minimal cost across the training set. Features can be engineered and analyzed in context of point set matching just as in traditional supervised learning tasks.

Features are expressed as attributes over hyperedge multiplicities $d = 1, 2, \dots, n$. Hyperedge features $g_s^{(d)}$, $s = 1, \dots, n_d$ are given as input. Each feature $g_s^{(d)}$ assumes a Gaussian distribution, and if $n_d \geq 2$ the features are modeled as a multivariate Gaussian distribution. Measurements from the data are used to derive estimates of the parameters of the Gaussian distributions. The most common application in heuristic approaches is to use the previous frame's feature values as the centers of the distributions. This standard approach is effective for simple lower variance features. However, higher degree features may have more variation frame-to-frame. Mean estimates across the training data can better account for macroscopic patterns in more complex features. The variances are then estimated from the feature values across the training set. The dissimilarity costs arise from functions attributed to hyperedges quantified by parametric assumptions.

The dissimilarity tensors $\mathbf{Z}^{(d)}$ can now be expressed as a function of the n_d features of hyperedge d . A partial assignment up to degree d : $[(l_1, \dots, l_d) \mapsto (l'_1, \dots, l'_d)]$ invokes

a cost according to the n_d features: $\sum_{s=1}^{n_d} g_s^{(d)}$. The expected values: $\sum_{s=1}^{n_d} \bar{g}_s^{(d)}$ are calculated in aggregate from training data for higher variance patterns:

$$\bar{g}_s^{(d)} = \frac{\sum_{L=1}^N g_s^{(d)}(X_L, \mathbf{X}_L)}{N} \quad (20)$$

where X_L and \mathbf{X}_L are the correct permutation and observed point set, respectively, for sample L . The variance-covariance matrix uses estimated means to estimate variances and covariances among feature measurements in the annotated data:

$$\hat{\sigma}_{a,b}^{(d)} = \sum_{L=1}^N (g_a^{(d)}(X_L, \mathbf{X}_L) - \bar{g}_a^{(d)})(g_b^{(d)}(X_L, \mathbf{X}_L) - \bar{g}_b^{(d)}) \quad (21)$$

$$\hat{\Sigma}_g^{(d)} = \left[\begin{array}{cccc} \hat{\sigma}_{1,1}^{(d)} & \hat{\sigma}_{1,2}^{(d)} & \dots & \hat{\sigma}_{1,n_d}^{(d)} \\ \hat{\sigma}_{2,1}^{(d)} & \hat{\sigma}_{2,2}^{(d)} & \dots & \hat{\sigma}_{2,n_d}^{(d)} \\ \dots & \dots & \dots & \dots \\ \hat{\sigma}_{n_d,1}^{(d)} & \hat{\sigma}_{n_d,2}^{(d)} & \dots & \hat{\sigma}_{n_d,n_d}^{(d)} \end{array} \right] \underbrace{n \times n, \dots, \times n}_{2d}$$

The selection rule tensor dissimilarity tensors $\mathbf{Z}^{(d)} \in R^{\underbrace{n \times n, \dots, \times n}_{2d}}$ use both sets of estimates to compute costs. The Mahalanobis distance is used to describe the scaled distance between the observed attributed hyperedge to an estimated feature description. Let $\mathbf{g}^{(d)} = [g_1^{(d)}, g_2^{(d)}, \dots, g_{n_d}^{(d)}]'$ and $\bar{\mathbf{g}}^{(d)} = [\bar{g}_1^{(d)}, \bar{g}_2^{(d)}, \dots, \bar{g}_{n_d}^{(d)}]'$

$$\mathbf{Z}_{l_1 l'_1 l_2 l'_2 \dots l_d l'_d}^{(d)} = (\mathbf{g}^{(d)} - \bar{\mathbf{g}}^{(d)})' (\hat{\Sigma}_g^{(d)})^{-1} (\mathbf{g}^{(d)} - \bar{\mathbf{g}}^{(d)}) \quad (22)$$

C. elegans Posture Modeling This section aims to introduce feature visualizations and discuss the effectiveness of various features for identifying the correct seam cell nuclei assignment.

Consider an image captured at time t with $n = 20$ located nuclei centroids. The coordinates can be stored as $\mathbf{X} \in R^{n,3}$ which $\mathbf{X}_i = [x_i, y_i, z_i]$ representing the i^{th} centroid in R^3 . Then let 1, 3, 5, ..., 19 be in the indices of the left side, and 2, 4, 6, ..., 20 be the indices of the right side. Then the cell nuclei are paired (1, 2) for the tail pair, then (2, 3), (4, 5), (6, 7), ..., (19, 20) for the body pairs. Let $\mathbf{L} = (l_1, l_2, \dots, l_m)$ denote the left side locations, and similarly \mathbf{R} the right.

The sampled worm embryos tend to develop at similar rates. However, the occurrence of the first twitch, a point in development that triggers rapid physical changes, varies embryo to embryo. Thus a time normalization is applied in effort to compare data from the different samples. Each worm's time to first twitch is measured s_w , as well as hatch time h_w for worm $w = 1, 2, \dots, 10$. The time points for each sample are indexed $k = 1, 2, \dots, n_w$. Now, each volume's imaging time t_{wk} is normalized to the $[0, 1]$ scale via the following formula:

$$z_{wk} = \frac{t_{wk} - s_w}{h_w - s_w}$$

Each time point $z_{wk} \in [0, 1]$ is scaled such that $z_{wk} = 0$ represents first twitch, and $z_{wk} = 1$ hatching. All plots will feature the normalized time of observation z_{wk} on the horizontal axis. The y axis unit will vary plot to plot. Distances will be measured in microns, μm , angles measured in degrees, $\theta \in [0, 360]$. Plots with multiple subplots will measure pairwise features, features defined by linking a length two sequence of pairs, or features defined by a length three sequence of pairs. The leftmost plot will depict features for the tail or sequence starting from the tail, while the rightmost will depict the feature ending with the head pair, at the anterior of the worm. Features are

calculated conditioned on stage of development in binned intervals of length .05 as well as the region in the worm measured by pair index.

QAP The quadratic model uses scaled distances between pairs of nuclei. The first feature to analyze is the distance between paired cell nuclei (Fig 9-A):

$$\mathbf{PD}_i = \|\mathbf{L}_i - \mathbf{R}_i\|_2 \quad (23)$$

This can be biologically interpreted as the width of the worm measured at the sampled nuclei locations. As mentioned above, the first subplot illustrates distances in microns between nuclei centroids of the tail pair for each observation. The distance between nuclei in the tail pair (left-most panel) is used for the initial pair selection rule H_1 across all models. The second set of distances form along the left and right sides of the worm (Fig 9-B). The lengths of chords between successive nuclei on each side are calculated: $\|\mathbf{L}_{i+1} - \mathbf{L}_i\|_2$ and $\|\mathbf{R}_{i+1} - \mathbf{R}_i\|_2$. Similar to the pair distances, side length observations are highly variant.

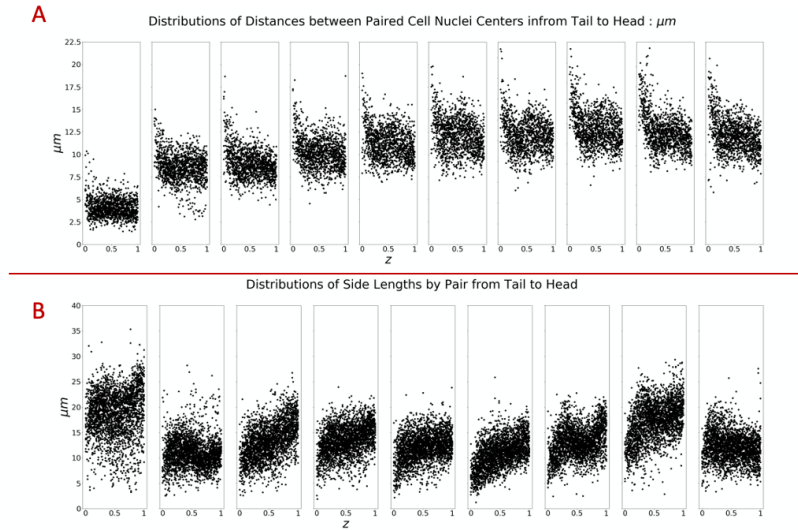


Fig 9. QAP model features. A) Distances between nuclei of lateral pairs. Notably, the tail pair distance (left-most panel) is constant throughout imaging. The tail pair distance informs the initial pair selection rule H_1 . B) Chord lengths along left and right sides of the posture. Both quadratic features show high variance.

Pairs The *Pairs* model uses hyperedges connecting two or three pairs of nuclei (four or six nuclei). The first four features measure pair-to-pair variation, while the latter two features use triplets of pairs to measure angles formed by the midpoints of the three pairs. The first pair-to-pair feature extends upon the use of pair distances to better describe the coiled worm. The ratio of sequential pair distances models the variation in width throughout the assigned nuclei (Fig 10-A):

$$PDR_i = \frac{PD_i}{PD_{i+1}} \quad (24)$$

Each feature's estimated mean is slightly greater than 1, indicating that, on average, the worm is widening from tail to head. Another easily interpreted distance is the length

of the chords connecting sequential pair midpoints. This is a more robust measure of worm length as side lengths vary more based upon the worm's folding (Fig 10-B):

$$MD_i = \|\mathbf{M}_{i+1} - \mathbf{M}_i\|_2 \quad (25)$$

The length of the chords connecting sequential pair midpoints is a more robust measure of worm length as side lengths vary more based upon the worm's folding. The cosine similarity is used to assess the degree to which sequential sides are pointing in the same direction (Fig 10-C):

$$\phi_i = \frac{(\mathbf{R}_{i+1} - \mathbf{R}_i) \cdot (\mathbf{L}_{i+1} - \mathbf{L}_i)}{\|\mathbf{R}_{i+1} - \mathbf{R}_i\|_2 \|\mathbf{L}_{i+1} - \mathbf{L}_i\|_2} \in [-1, 1] \quad (26)$$

The final two pair-to-pair *Pairs* features attempt to model two different types of *twist* in the posture. The lateral and axial twists measures angles of rotation from lateral and posterior views, respectively (Fig 10-D).

$$\mathbf{b}_1 = \frac{\mathbf{L}_{i+1} - \mathbf{L}_i}{\|\mathbf{L}_{i+1} - \mathbf{L}_i\|_2} \quad (27)$$

$$\mathbf{b}_2 = \frac{\mathbf{L}_i - \mathbf{R}_i}{\|\mathbf{L}_i - \mathbf{R}_i\|_2} \quad (28)$$

$$\mathbf{b}_3 = \frac{\mathbf{R}_i - \mathbf{R}_{i+1}}{\|\mathbf{R}_i - \mathbf{R}_{i+1}\|_2} \quad (29)$$

$$\mathbf{b}_4 = \frac{\mathbf{R}_{i+1} - \mathbf{L}_{i+1}}{\|\mathbf{R}_{i+1} - \mathbf{L}_{i+1}\|_2} \quad (30)$$

$$\mathbf{n}_1 = \mathbf{b}_1 \times \mathbf{b}_2 \quad (31)$$

$$\mathbf{n}_2 = \mathbf{b}_2 \times \mathbf{b}_3 \quad (32)$$

$$\mathbf{n}_3 = \mathbf{b}_3 \times \mathbf{b}_4 \quad (33)$$

$$\mathbf{c}_1 = \langle \mathbf{n}_1 \times \mathbf{n}_2, \mathbf{b}_2 \rangle \quad (34)$$

$$\mathbf{c}_2 = \langle \mathbf{n}_1, \mathbf{n}_2 \rangle \quad (35)$$

$$\psi_i = \frac{1}{\pi} \text{atan}2(\langle \mathbf{n}_1 \times \mathbf{n}_2, \mathbf{b}_2 \rangle, \langle \mathbf{n}_1, \mathbf{n}_2 \rangle) \quad (36)$$

$$(37)$$

Axial twists present between a sequence of two pairs calculates the angle obtained by projecting the chord linking pairs onto each other (Fig 10-E):

$$\mathbf{b}_1 = \frac{\mathbf{L}_i - \mathbf{L}_{i+1}}{\|\mathbf{L}_i - \mathbf{L}_{i+1}\|_2} \quad (38)$$

$$\mathbf{b}_2 = \frac{\mathbf{R}_i - \mathbf{L}_i}{\|\mathbf{R}_i - \mathbf{L}_i\|_2} \quad (39)$$

$$\mathbf{b}_3 = \frac{\mathbf{R}_{i+1} - \mathbf{R}_i}{\|\mathbf{R}_{i+1} - \mathbf{R}_i\|_2} \quad (40)$$

$$\mathbf{b}_4 = \frac{\mathbf{L}_{i+1} - \mathbf{R}_{i+1}}{\|\mathbf{L}_{i+1} - \mathbf{R}_{i+1}\|_2} \quad (41)$$

$$\mathbf{n}_1 = \mathbf{b}_1 \times \mathbf{b}_2 \quad (42)$$

$$\mathbf{n}_2 = \mathbf{b}_2 \times \mathbf{b}_3 \quad (43)$$

$$\mathbf{n}_3 = \mathbf{b}_3 \times \mathbf{b}_4 \quad (44)$$

$$\mathbf{c}_1 = \langle \mathbf{n}_2 \times \mathbf{n}_3, \mathbf{b}_3 \rangle \quad (45)$$

$$\mathbf{c}_2 = \langle \mathbf{n}_2, \mathbf{n}_3 \rangle \quad (46)$$

$$\tau_i = \frac{1}{\pi} \text{atan2}(\langle \mathbf{n}_2 \times \mathbf{n}_3, \mathbf{b}_3 \rangle, \langle \mathbf{n}_2, \mathbf{n}_3 \rangle) \quad (47)$$

$$(48)$$

Angles along sides of the worm formed by triples of sequential nuclei approximate bend in the worm along each side. These angles are highly variant, in the same manner as side lengths in *QAP* (Fig 9-B). Angles formed by pair midpoints exacerbate the computational burden as six nuclei are required, compare to three in a typical angle calculation, but the midpoint based angles are less variant than angles of each side (Fig 10-F):

$$\Theta_i = \frac{180}{\pi} \arccos \frac{\langle \mathbf{M}_{i+1} - \mathbf{M}_i, \mathbf{M}_{i+2} - \mathbf{M}_{i+1} \rangle}{\|\mathbf{M}_{i+1} - \mathbf{M}_i\|_2 \|\mathbf{M}_{i+2} - \mathbf{M}_{i+1}\|_2} \quad (49)$$

Each angle $\Theta \in [0, 180]$ where 0 would denote the worm perfectly folded upon itself, and 180 would define a flat worm. A second set of angles aims to approximate the posterior to anterior bend in the worm. The angles ζ_i are defined as the angles formed by fitted planes intersecting between pair midpoints (Fig 10-G):

$$\zeta_i = \frac{180}{\pi} \frac{\langle (\mathbf{R}_{i+1} - \mathbf{L}_{i+1}) \times (\mathbf{M}_{i+1} - \mathbf{M}_i), ((\mathbf{R}_{i+1} - \mathbf{L}_{i+1}) \times (\mathbf{M}_{i+1} - \mathbf{M}_{i+1})) \rangle}{\|(\mathbf{R}_{i+1} - \mathbf{L}_{i+1}) \times (\mathbf{M}_{i+1} - \mathbf{M}_i)\|_2 \|(\mathbf{R}_{i+1} - \mathbf{L}_{i+1}) \times (\mathbf{M}_{i+1} - \mathbf{M}_{i+1})\|_2} \quad (50)$$

Posture The *Posture* model is comprised of all *Pairs* features as well as the features defined by the summations of each local feature measurement throughout the hypothesized posture. Full posture features give insight into the changes in the embryo's shape throughout late-stage embryogenesis (Fig 11). Worm length follows an approximately logarithmic pattern. Total curvature follows a negative exponential pattern. Earlier on the worm is fatter and cannot bend as much. The worm elongates during development, allowing for sharper bends.

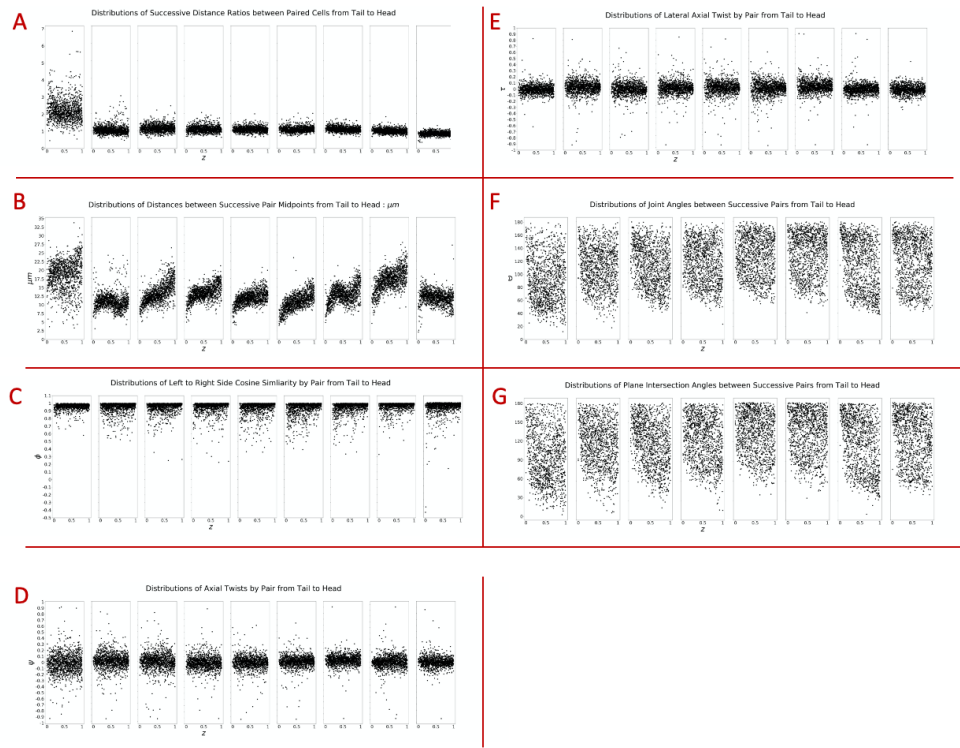


Fig 10. Pairs model features. A) Ratios of pair distances (Eq 24). B) Distance between successive pair midpoints (Eq 25. C) Cosine similarities between successive left and right sides (Eq 26. D) Lateral axial twist angles (Eq 27). E) Axial twist angles (Eq 38). F) Midpoint bend angles (Eq 49. G) Planar intersection angles (Eq 50).

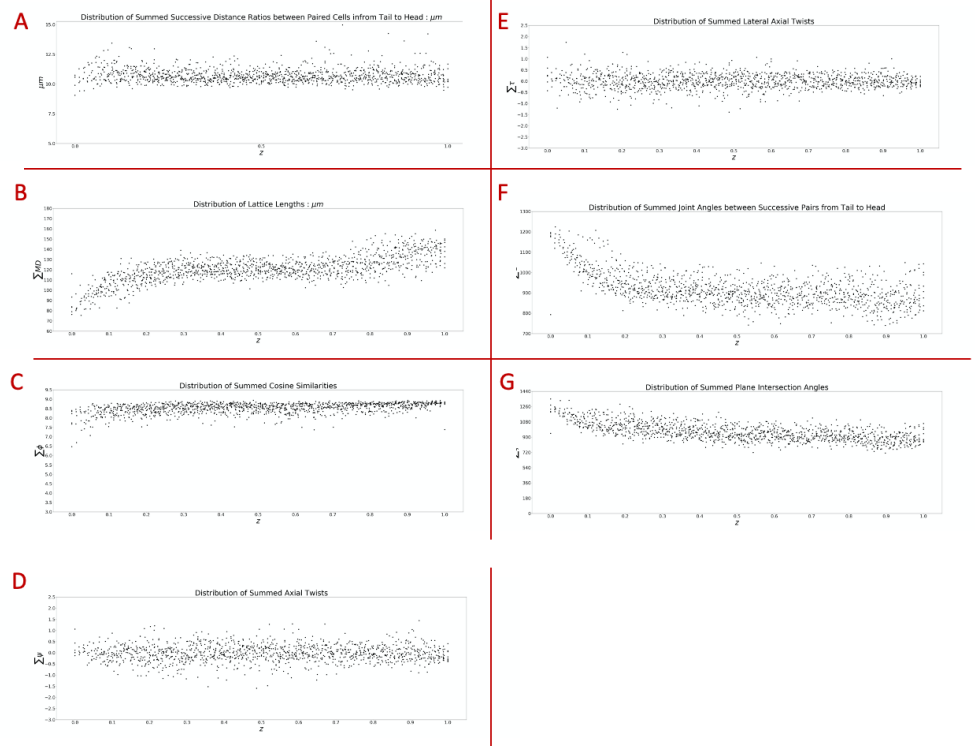


Fig 11. Posture model features include all *Pairs* features and posture-wide versions of *Pairs* features. A) Summed ratios of pair distances (Eq 24). B) Summed distances between successive pair midpoints (Eq 25. C) Summed cosine similarities between successive left and right sides (Eq 26. D) Summed lateral axial twist angles (Eq 27). E) Summed axial twist angles (Eq 38). F) Summed midpoint bend angles (Eq 49. G) Summed planar intersection angles (Eq 50).

References

1. Zhou F, Torre FDL. Factorized Graph Matching. *IEEE Transactions on Pattern Analysis and Machine Intelligence*. 2016;38(9):1774–1789. doi:10.1109/TPAMI.2015.2501802.
2. Zhang Z, Xiang Y, Wu L, Xue B, Nehorai A. KerGM: Kernelized Graph Matching. In: Wallach H, Larochelle H, Beygelzimer A, Alché-Buc F, Fox E, Garnett R, editors. *Advances in Neural Information Processing Systems*. vol. 32. Curran Associates, Inc.; 2019. Available from: <https://proceedings.neurips.cc/paper/2019/file/cd63a3eec3319fd9c84c942a08316e00-Paper.pdf>.
3. Duchenne O, Bach F, Kweon IS, Ponce J. A Tensor-Based Algorithm for High-Order Graph Matching. *IEEE TRANSACTIONS ON PATTERN ANALYSIS AND MACHINE INTELLIGENCE*. 2010; p. 13.
4. Chertok M, Keller Y. Efficient High Order Matching. *IEEE Transactions on Pattern Analysis and Machine Intelligence*. 2010;32(12):2205–2215. doi:10.1109/TPAMI.2010.51.
5. Lee J, Cho M, Lee KM. Hyper-graph matching via reweighted random walks. In: *CVPR 2011*; 2011. p. 1633–1640.
6. White JG, Southgate E, Thomson JN, Brenner S. The structure of the nervous system of the nematode *Caenorhabditis elegans*. *Philosophical Transactions of the Royal Society of London B, Biological Sciences*. 1986;314(1165):1–340. doi:10.1098/rstb.1986.0056.
7. Sulston JE, Schierenberg E, White JG, Thomson JN. The embryonic cell lineage of the nematode *Caenorhabditis elegans*. *Developmental Biology*. 1983;100(1):64–119. doi:10.1016/0012-1606(83)90201-4.
8. Chisholm AD, Hutter H, Jin Y, Wadsworth WG. The Genetics of Axon Guidance and Axon Regeneration in *Caenorhabditis elegans*. *Genetics*. 2016;204(3):849–882. doi:10.1534/genetics.115.186262.
9. Rapti G. A perspective on *C. elegans* neurodevelopment: from early visionaries to a booming neuroscience research. *Journal of Neurogenetics*. 2020;34(3-4):259–272. doi:10.1080/01677063.2020.1837799.
10. Christensen RP, Bokinsky A, Santella A, Wu Y, Marquina-Solis J, Guo M, et al. Untwisting the *Caenorhabditis elegans* embryo. *eLife*. 2015;4:e10070. doi:10.7554/eLife.10070.
11. Sahni S, Gonzales T. P-complete problems and approximate solutions. In: *15th Annual Symposium on Switching and Automata Theory (swat 1974)*. USA: IEEE; 1974. p. 28–32. Available from: <http://ieeexplore.ieee.org/document/4569755/>.
12. McAuliffe MJ, Lalonde FM, McGarry D, Gandler W, Csaky K, Trus BL. Medical Image Processing, Analysis and Visualization in clinical research. In: *Proceedings 14th IEEE Symposium on Computer-Based Medical Systems*. CBMS 2001; 2001. p. 381–386.
13. Land AH, Doig AG. An Automatic Method of Solving Discrete Programming Problems. *Econometrica*. 1960;28(3):497–520. doi:10.2307/1910129.

14. Bao Z, Murray JI, Boyle T, Ooi SL, Sandel MJ, Waterston RH. Automated cell lineage tracing in *Caenorhabditis elegans*. *Proceedings of the National Academy of Sciences of the United States of America*. 2006;103(8):2707–2712. doi:10.1073/pnas.0511111103.
15. Boyle TJ, Bao Z, Murray JI, Araya CL, Waterston RH. AceTree: a tool for visual analysis of *Caenorhabditis elegans* embryogenesis. *BMC Bioinformatics*. 2006;7(1):275. doi:10.1186/1471-2105-7-275.
16. Santella A, Catena R, Kovacevic I, Shah P, Yu Z, Marquina-Solis J, et al. WormGUIDES: an interactive single cell developmental atlas and tool for collaborative multidimensional data exploration. *BMC Bioinformatics*. 2015;16(1):189. doi:10.1186/s12859-015-0627-8.
17. Mace DL, Weisdepp P, Gevirtzman L, Boyle T, Waterston RH. A High-Fidelity Cell Lineage Tracing Method for Obtaining Systematic Spatiotemporal Gene Expression Patterns in *Caenorhabditis elegans*. *G3: Genes, Genomes, Genetics*. 2013;3(5):851–863. doi:10.1534/g3.113.005918.
18. Cao J, Guan G, Ho VWS, Wong MK, Chan LY, Tang C, et al. Establishment of a morphological atlas of the *Caenorhabditis elegans* embryo using deep-learning-based 4D segmentation. *Nature Communications*. 2020;11(1):6254. doi:10.1038/s41467-020-19863-x.
19. Wang S, Ochoa SD, Khalilullin RN, Gerson-Gurwitz A, Hendel JM, Zhao Z, et al. A high-content imaging approach to profile *C. elegans* embryonic development. *Development*. 2019;146(7). doi:10.1242/dev.174029.
20. Wu Y, Wawrzusin P, Seneney J, Fischer RS, Christensen R, Santella A, et al. Spatially isotropic four-dimensional imaging with dual-view plane illumination microscopy. *Nature Biotechnology*. 2013;31(11):1032–1038. doi:10.1038/nbt.2713.
21. Valdivia P, Buono P, Plaisant C, Dufournaud N, Fekete JD. Analyzing Dynamic Hypergraphs with Parallel Aggregated Ordered Hypergraph Visualization. *IEEE Transactions on Visualization and Computer Graphics*. 2021;27(1):1–13. doi:10.1109/TVCG.2019.2933196.